FACULTY
OF MATHEMATICS
AND PHYSICS
Charles University

MASTER THESIS

Burak Aygün

Tidal Deformation of an Icy Moon with a Subsurface Ocean

Mathematics

Supervisor of the master thesis: prof. RNDr. Ondřej Čadek, CSc

Study programme: Mathematics

Study branch: Mathematical Modelling in Physics
and Technology

Prague 2021

I declare that I carried out this master thesis independently, and only with the cited sources, literature and other professional sources. It has not been used to obtain another or the same degree.

I understand that my work relates to the rights and obligations under the Act No. 121/2000 Sb., the Copyright Act, as amended, in particular the fact that the Charles University has the right to conclude a license agreement on the use of this work as a school work pursuant to Section 60 subsection 1 of the Copyright Act.

In . . . . date . . . .

Author's signature

i

I dedicate this to my parents for always supporting me and trusting me. I also dedicate this to my supervisor prof. RNDr. Ondřej Čadek, CSc, for his patience, support and guidance throughout my studies.

Title: Tidal Deformation of an Icy Moon with a Subsurface Ocean

Author: Burak Aygün

Mathematical Institute of Charles University: Mathematics

Supervisor: prof. RNDr. Ondřej Čadek, CSc, Department of Geophysics

Abstract: Enceladus is one of the icy moons in the outer solar system. The Cassini mission has found out direct evidence on existing subsurface ocean. These evidences showed that the water contains organic molecules and nutrient, such that it could create suitable environment for emergence of life. However, the mechanism how the ocean is maintained in a liquid state, is still unknown. We studied the effect of the tidal force on maintaining the ocean in a liquid state, where the effect of the elastic ice shell is modelled through boundary condition. We modelled the ocean with the three dimensional linearised incompressible Navier-Stokes equations in the time domain. Then, we solved the equations numerically with spectral method. The numerical methods are written in to Fortran 90 program. We tested the various properties of the numerical methods. We, then, investigate the tidal dissipation for various ocean thicknesses and viscosities. We conclude that the tidal dissipation heavily depends on the thickness and the viscosity. These results show us that the tidal force could have significant contribution to the total heat budget of Enceladus for given viscosities of the ocean.

Keywords: Enceladus, Subsurface Ocean, Spectral Method, Tidal Dissipation

Contents

Introduction

Over the past two decades, observations of the Cassini-Huygens mission showed us that several icy moons of the outer solar system have liquid oceans underneath their ice shells (e.g. Europa, Enceladus, Io, Ganymede). These icy moons became an interesting subject due to their possibility of holding life. However, before exploring whether it is possible to find living forms in these oceans, it is equally important that we understand how these oceans are maintained. As presented in Nimmo and Pappalardo (2016), there are several mechanisms which maintain a liquid ocean under the ice shell, but we focus on tidal dissipation. In particular, we study the small moon of Saturn, Enceladus.

Through the observations from its south polar region, the Cassini spacecraft collected evidence showing that there is a subsurface ocean under the ice shell. From Thomas et al. (2016), we know that Enceladus' ocean is global and it separates the ice shell and the core. The total heat production of Enceladus is estimated around 15.8 ± 3.1 GW, where the estimated radiogenic heating is 0.3 GW (Howett et al., 2011; Porco et al., 2006). Therefore, it is evident that there must be another source of heat. One main source of heat production is considered to be tidal potential (Nimmo et al., 2018). Due to its orbit around Saturn, Enceladus is under the effect of time dependent tidal potential. The impact of the tidal potential on the icy moons is that it deforms the ice shell and the core, and creates flow within the ocean. However, it is not clear where the most dissipation appears. In the papers by Souček et al. (2016) and Souček et al. (2019), the effect of the ice shell on the total heat production is investigated. It is observed that the dissipation within the viscoelastic ice shell is concentrated on the south polar region. However, it is also clear that the dissipation from the ice shell would not be sufficient to keep the ocean liquid. Thus, the dissipation must come from either the core or the ocean. We assume that the core of Enceladus is rigid and does not deform. Hence, we focus on the heat produced by the ocean.

The impact of the tidal potential on the subsurface oceans might play a crucial role in keeping the ocean liquid. However, whether tidal potential would be enough to keep the oceans liquid is still unknown. Most of the previous studies

are carried out with shallow water approximation. The studies assumes that the horizontal flow scale is greater than the vertical flow scale. They, then, introduce the Laplace tidal equations (LTE) and carry out the computations (Vallis, 2017). In Matsuyama et al. (2018), an elastic ice shell on the top is assumed and tidal dissipation is investigated through LTE. It is found out that eccentricity tides can generate enough heat if the ocean is unrealistically thin. (Hay and Matsuyama, 2019) investigate the tidal dissipation due to non-linear drag. Their results show that the tidal dissipation with bottom drag is not sufficient to produce the heating that is observed. The heat production is still several orders smaller than the observed values. They found out, though, that obliquity tides produce more heat than the eccentricity tides. Moreover, in (Chen and Nimmo, 2011), we see that the obliquity tides do not play a substantial role in the total dissipation of Enceladus. (Matsuyama, 2014) shows that eccentricity tides might explain the heating of the ocean on Enceladus. They found that the heat flux from the eccentricity tides is couple of orders greater than the observed values, for the ocean with thickness of 1 km. They also conclude that the obliquity tides are not a significant source of heat, compared to eccentricity tides. Chen et al. (2014) discuss that the ocean tidal heating is not significant compared to the radiogenic heating, and dissipation occurs in solid parts of the moons, either in the ice shell or in the core. However, all the previously mentioned works use shallow water approximation, where the problems are formulated in two dimensions and the ocean is assumed to be in hydrostatic equilibrium. It is proposed in Rovira-Navarro et al. (2019) that three-dimensional approach can show the effect of the inertial waves on dissipation. The problem is modelled in the frequency domain and with linearised Navier-Stokes equations. Solving the equations with spectral methods, they conclude that the tidal heating is several orders smaller than the observed values for Enceladus.

In this thesis, we develop a three-dimensional model of the tidal dissipation problem in the time domain. We assume an elastic ice shell on the top boundary of the ocean. In order to solve the model, we employ spectral methods and write two programs in Fortran 90. The first program is to solve the elastic equations in order to find the top boundary condition for the ocean. The second program

is to solve the linearised Navier-Stokes equations. The organization of the thesis is as follows: in the first chapter, we introduce the governing equations, make the necessary simplifications, introduce the numerical schemes, both temporal and spatial, and present the numerical properties of the schemes. In the second chapter, we present the results for tidal dissipation depending on viscosity and thickness, and compare them with Rovira-Navarro et al. (2019). Then we discuss the results and conclude the thesis.

1. Methodology

The objective of this thesis is to develop a three dimensional model to describe the tidal dissipation in icy moons with subsurface oceans. The model explores the dissipation in the ocean caused by the tidal deformation of the ice shell. We consider a simplified linear model where the ocean and ice shell is decoupled and the affect of ice shell is prescribed through a boundary condition on the top surface of the ocean. As it can be seen from figure 1.1, we denote the two spatial domains corresponding to the ocean and ice shell as Ω_w and Ω_i, respectively, and we assume that the icy moon has a perfectly spherical geometry.
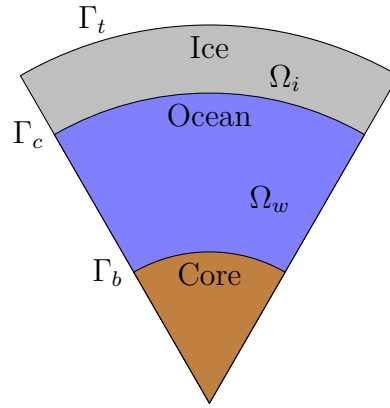

Figure 1.1: The computation domain is separated into two parts, Ω_i and Ω_w, corresponding to the ice shell and the ocean, respectively

1.1 Governing equations

The model is based on two fundamental balance laws of continuum mechanics (Málek and Průša, 2016). The first one is the balance of mass,

$$\frac{\partial \rho}{\partial t} + \operatorname{div}(\rho \boldsymbol{v}) = 0, \tag{1.1}$$

and the second one is the balance of linear momentum,

$$\rho \left(\frac{\partial \boldsymbol{v}}{\partial t} + \boldsymbol{v} \cdot \nabla \boldsymbol{v} \right) = \operatorname{div}\mathbb{T} + \boldsymbol{b} - 2\rho \boldsymbol{\omega} \times \boldsymbol{v}, \tag{1.2}$$

where t is the time, ρ is the density of water, $\boldsymbol{v}$ is the velocity, $\mathbb{T}$ is the Cauchy stress tensor, $\boldsymbol{b}$ is the external body force, $\boldsymbol{\omega}$ is the angular frequency and the last

term in equation (1.2) is the Coriolis force. Since the ocean is incompressible, and we consider a linearized model, the governing equations (1.1) and (1.2) take the following forms:

$$\text{div}\boldsymbol{v} = 0, \qquad\qquad \text{in} \quad Q_w \qquad (1.3a)$$

$$\rho\frac{\partial \boldsymbol{v}}{\partial t} = \text{div}\mathbb{T} + \boldsymbol{b} - 2\rho\boldsymbol{\omega} \times \boldsymbol{v}, \qquad \text{in} \quad Q_w \qquad (1.3b)$$

where $Q_w = \Omega_w \times [0, T_f]$ and $T_f > 0$ is the final time. The external body force can be expressed in terms of the tidal potential V,

$$\boldsymbol{b} = -\rho\nabla V, \qquad\qquad (1.4)$$

with

$$V(t, r, \theta, \phi) = r^2\omega^2 e\Big[P_{20}(\cos\theta)\cos\omega t + $$
$$P_{22}(\cos\theta)\left(3\cos\omega t\cos 2\phi + 4\sin\omega t\sin 2\phi\right)\Big], \qquad (1.5)$$

where r, θ, ϕ are the spherical coordinates, e is the eccentricity and P_{20} and P_{22} are the associated Legendre polynomials of degree 2, order 0 and 2, respectively. Moreover, the Cauchy stress tensor $\mathbb{T}$ satisfies the following constitutive equation

$$\mathbb{T} = -p\mathbb{I} + \eta\left(\nabla\boldsymbol{v} + (\nabla\boldsymbol{v})^T\right), \qquad (1.6)$$

where p is the pressure and η is the viscosity.

1.2   Boundary conditions

We assume no slip boundary condition on the bottom of the ocean, where it is in contact with the core, i.e.,

$$\boldsymbol{v} = \boldsymbol{0} \quad \text{on} \ \ \Gamma_b. \qquad (1.7)$$

On the top boundary of the ocean we assume that the surface deforms accordingly to the deformation of the ice shell. Therefore, we prescribe the normal component of the traction vector as

$$(\mathbb{T}\boldsymbol{n}) \cdot \boldsymbol{n} = -u_r\left(\rho - \rho_i\right)g \quad \text{on} \ \ \Gamma_c, \qquad (1.8)$$

and the tangential velocity as

$$\boldsymbol{v} - (\boldsymbol{v} \cdot \boldsymbol{n})\,\boldsymbol{n} = \boldsymbol{0} \quad \text{on} \ \ \Gamma_c, \tag{1.9}$$

where $u_r = \boldsymbol{u} \cdot \boldsymbol{n}$ is the normal component of the displacement of the ice shell, ρ_i is the density of the ice, g is the gravitational acceleration and $\boldsymbol{n}$ is the unit outward vector. The displacement $\boldsymbol{u}$ is the solution to the system which governs the deformation of the ice shell due to the tidal forces. In this system, we assume that ice shell is elastic, incompressible and its deformation is small. Thus, according to these assumptions we have the following system

$$\text{div}\,\boldsymbol{u} = 0, \qquad\qquad \text{in} \ \ \Omega_i \tag{1.10a}$$

$$\text{div}\,\mathbb{S} = \boldsymbol{b}, \qquad\qquad \text{in} \ \ \Omega_i \tag{1.10b}$$

where $\mathbb{S}$ is the Cauchy stress tensor in the ice shell and $\boldsymbol{b} = \rho_i \nabla V$. Moreover, $\mathbb{S}$ satisfies the following constitutive equation:

$$\mathbb{S} = -p_i \mathbb{I} + \mu \left(\nabla \boldsymbol{u} + (\nabla \boldsymbol{u})^T \right) \tag{1.11}$$

where p_i is the pressure in the ice and μ is the shear modulus. We assume that the top boundary of the ice shell is stress free and the deformation is small, which implies that the boundary condition can be written in the reference configuration as follows

$$\mathbb{S}\boldsymbol{n} = -u_r \rho_i g \boldsymbol{n} \quad \text{on} \ \Gamma_t. \tag{1.12}$$

For the bottom boundary of the ice shell, i.e. the boundary separating the ice domain from the water ocean, we assume that the ocean is in hydrostatic state,and we take into account the pressure due to the tidal potential in the ocean. The bottom boundary condition in the reference configuration then takes the following form

$$-\mathbb{S}\boldsymbol{n} + u_r \left(\rho - \rho_i \right) g \boldsymbol{n} = -\rho V \boldsymbol{n} \quad \text{on} \ \Gamma_c. \tag{1.13}$$

1.3   Time integration

For the system (1.3)-(1.6), we split the (1.3b) into two parts: the part that we can treat implicitly, $I(t)$, and the part that we treat explicitly, $E(t)$. Thus, we

rewrite equation (1.3b) as

$$-\rho\frac{\partial \boldsymbol{v}}{\partial t} = -I\left(t\right) + E\left(t\right), \tag{1.14}$$

where $E\left(t\right) = 2\rho\boldsymbol{\omega} \times \boldsymbol{v}$ and $I\left(t\right) = \mathrm{div}\mathbb{T} + \boldsymbol{b}$. Then for the implicit part we employ θ-scheme where $\theta \in [0,1]$ and for the explicit part we employ the 3rd order Adams-Bashforth method (Griffiths and Higham, 2010). Therefore, we can write the discrete form of (1.14) as follows

$$\begin{aligned}
-\rho\frac{\boldsymbol{v}_{k+1}}{\Delta t} + \theta I\left(t_{k+1}\right) &= -\rho\frac{\boldsymbol{v}_k}{\Delta t} - \left(1-\theta\right)I\left(t_k\right) \\
&+ \left(\frac{23}{12}E\left(t_k\right) - \frac{16}{12}E\left(t_{k-1}\right) + \frac{5}{12}E\left(t_{k-2}\right)\right)
\end{aligned} \tag{1.15}$$

where $\Delta t = t_{k+1} - t_k$ is the time step and $k = 1, 2, \dots$. It is observed that when $\theta \leq 0.5$, the numerical scheme produces unstable results and, therefore, we use the values $\theta > 0.5$ in computations.

1.4   Spatial discretization

The spatial discretization is the same for both the ice shell and the ocean, therefore we will explain only for the ocean model. We prescribe finite difference approximation on a staggered grid for each time instant t_k, where $k = 1, 2, \dots$. In order to discretize the governing equations we first write them in terms of spherical harmonics (Appendix A.1) and obtain a system of ordinary differential equations which depend on radius. Then, as shown in figure 1.2, we prescribe the stress field on interfaces along with the equation of balance of mass, whereas the velocity field and the equation of balance of linear momentum are prescribed in the middle of the layers. We use homogeneous spatial discretization with the spatial step

$$\Delta r = \frac{r_t - r_b}{n-1}, \tag{1.16}$$

where r_t and r_b are the top and the bottom radius of the ocean, respectively, and n is the number of interfaces. Then, the discretization takes the following form:

$$\begin{aligned}
r_{i+1} &= r_i + \Delta r \quad \text{for} \quad i = 2, \dots, n-1, \\
\tilde{r}_{i+1} &= \tilde{r}_i + \Delta r \quad \text{for} \quad i = 2, \dots, n,
\end{aligned} \tag{1.17}$$

where $r_1 = r_b$ and $\tilde{r}_1 = r_1 - \frac{\Delta r}{2}$.
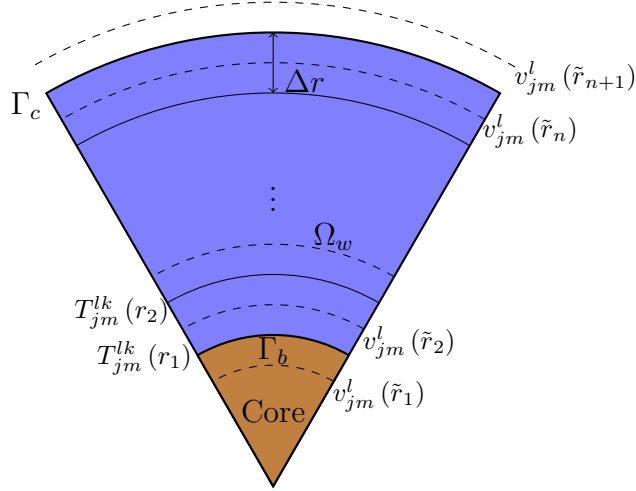
Figure 1.2: Spatial discretization of the domain of the ocean, Ω_w.

Therefore, we can approximate the derivative of velocity and stress fields as

$$\begin{aligned}
\frac{\mathrm{d}v_{jm}^l(r_i)}{\mathrm{d}r} &= \frac{v_{jm}^l(\tilde{r}_{i+1}) - v_{jm}^l(\tilde{r}_i)}{\Delta r}, \\
\frac{\mathrm{d}T_{jm}^{lk}(\tilde{r}_i)}{\mathrm{d}r} &= \frac{T_{jm}^{lk}(r_{i+1}) - T_{jm}^{lk}(r_i)}{\Delta r},
\end{aligned} \tag{1.18}$$

where v_{jm}^l and T_{jm}^{lk} are the spherical harmonic coefficients, which depends on radius.

1.5 Numerical Tests

In the following section, various numerical aspects of the method will be studied. The numerical schemes described above, are written into a program of Fortran 90. The numerical aspects will be studied in order to test the accuracy and efficiency of this program. We will investigate the parameters, such as time and spatial step, and cut-off degree. These parameters is investigated to determine the convergence properties of the numerical schemes. Numerical parameters of the system, depends on the value of viscosity. For higher values of viscosities, we can use lower resolution in the model. However, as the values of viscosity decreases, we require higher resolutions.

We make the computation for the viscosities between $\eta = 10^6$-10^3 Pa·s. The lower values of viscosities requires such high resolutions that the computations

become too cumbersome, where the values less than $\eta = 1$ Pa·s requires resolutions that we can not attain. Thus, we can not obtain high enough resolution to compute the realistic value of viscosity of water, $\eta = 10^{-3}$ Pa·s.

In all the computations, we use constant spatial and time step. Therefore, to ensure the numerical stability and increase the accuracy of the method, we employ the 3rd order Adams-Bashforth method, given as in equation (1.15). Using this method allows us to maintain numerically stable solution for higher values of time and spatial steps.

Outer radius	252.1 km
Radius of ice/water boundary	232.1 km
Core radius	194.1 km
Shear modulus of the ice (μ)	3.3 10^9 Pa
Period (T)	118387 s
Eccentricity (e)	0.0047
Gravitational acceleration (g)	0.113 m/s^2
Density of ice (ρ_i)	925 kg/m^3
Density of ocean (ρ)	1000 kg/m^3
Viscosity of the water (η)	10^6-10^3 Pa·s

Table 1.1: Parameters of Enceladus

In order to investigate numerical aspects of the method, we use the parameters of Enceladus, given in Table 1.1, and we look time evolution of the dissipation value, defined as

$$D\left(t\right) := \int_{\Omega_w} \frac{\mathbb{T}^d : \mathbb{T}^d}{2\eta} dx, \tag{1.19}$$

where $\mathbb{T}^d$ is the deviatoric part of the Cauchy stress tensor and

$$\mathbb{T}^d : \mathbb{T}^d = \sum_{i=1}^{3}\sum_{j=1}^{3} T_{ij}^{d\,2}. \tag{1.20}$$

The system is under the effect of periodic tidal force, therefore it is expected that the dissipation value over time would be steady periodic curve. However, due to the initial value, that is prescribed as $\boldsymbol{v} = \boldsymbol{0}$, we observe a transition regime

first, and afterwards, we can see the steady periodic behaviour, as it can be seen from Figures 1.3a - 1.3d. For higher values of viscosity, the transition regime is short and the system reaches the steady regime in small number of periods, see Figure 1.3a. As viscosity decreases, we can observe that, the system requires more number of periods to reach steady solution, see Figures 1.3b-1.3d. The necessary number of periods to obtain a steady solution for even lower viscosities can increase dramatically, for example, $\eta = 10$ Pa·s requires almost 1000 periods.
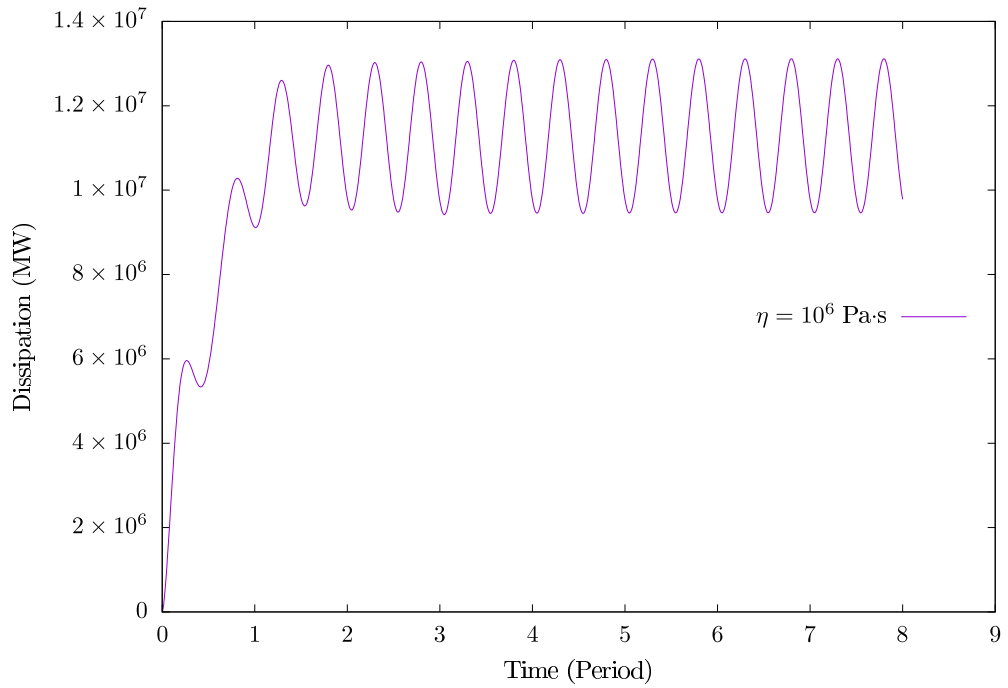
(a) $\eta = 10^6$ Pa·s
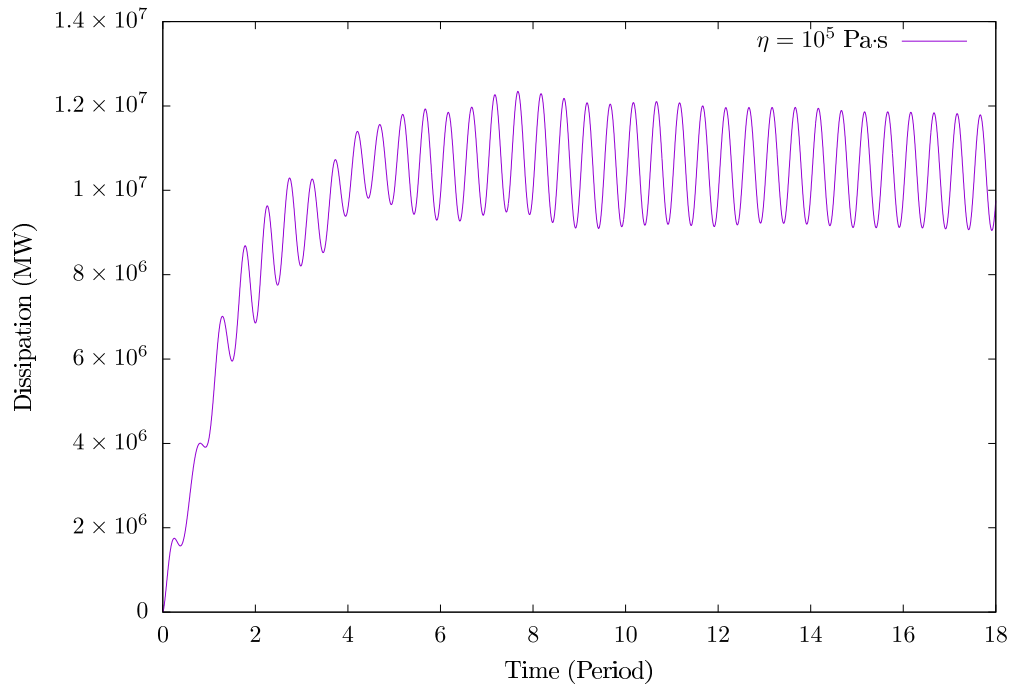
(b) $\eta = 10^5$ Pa·s
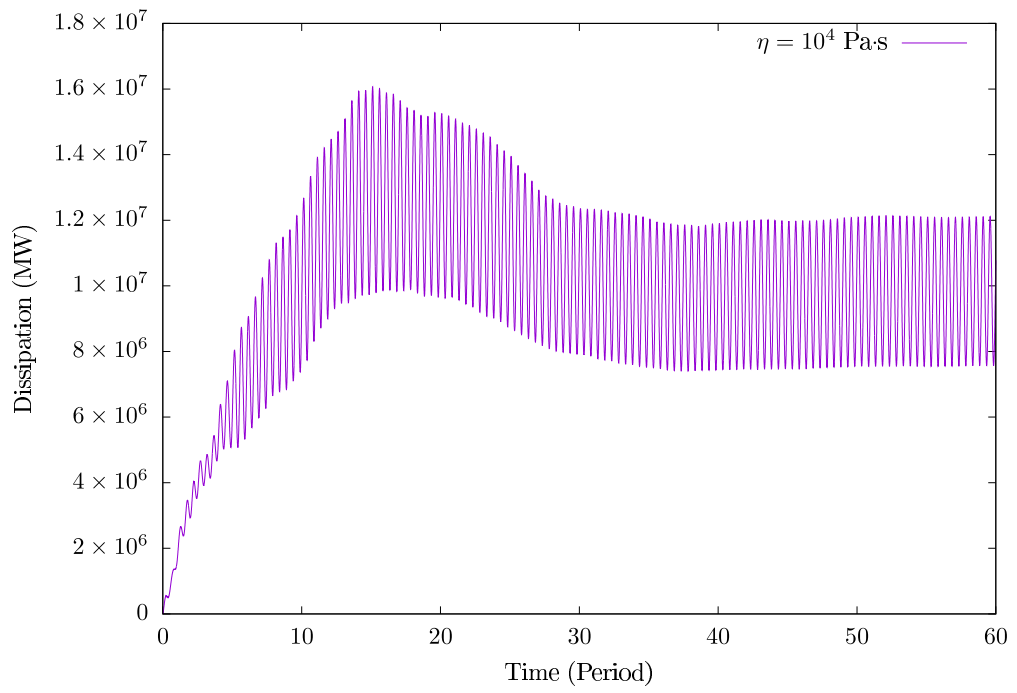
(c) $\eta = 10^4$ Pa·s
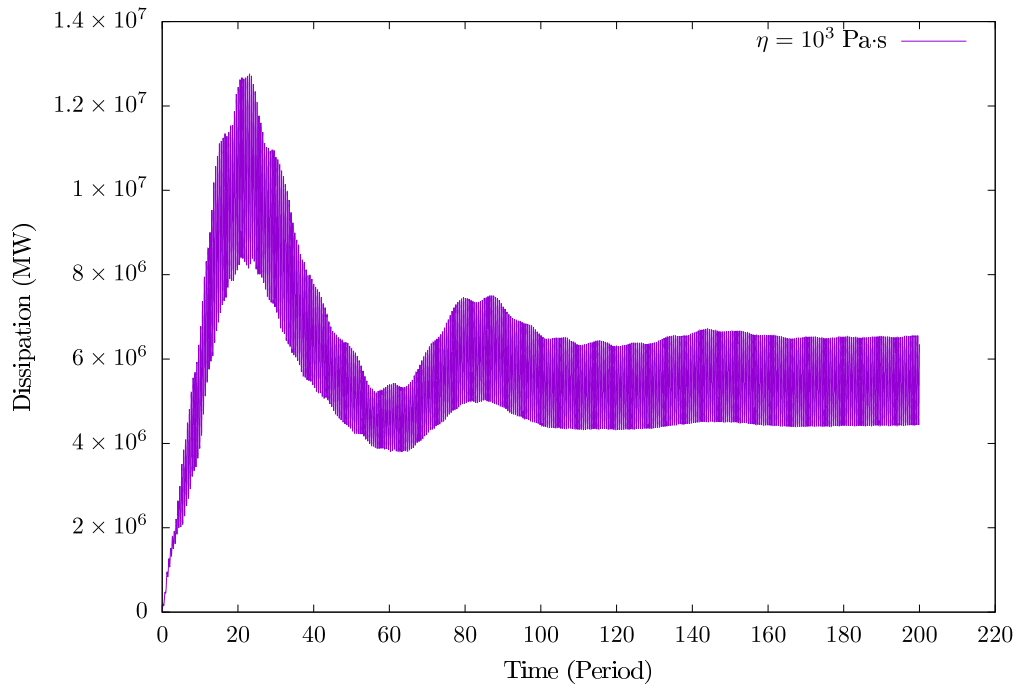
(d) $\eta = 10^3$ Pa·s

Figure 1.3: Stability of the system

Once the steady solution is reached, to investigate the convergence behaviour of the system for time step, we fix the value of the spatial step and compute several time steps. For each viscosity, we plot the dissipation curve over one period and compare the curves. As we can see from Figures 1.4a-1.4d, the dissipation curves converge as Δt decreases.
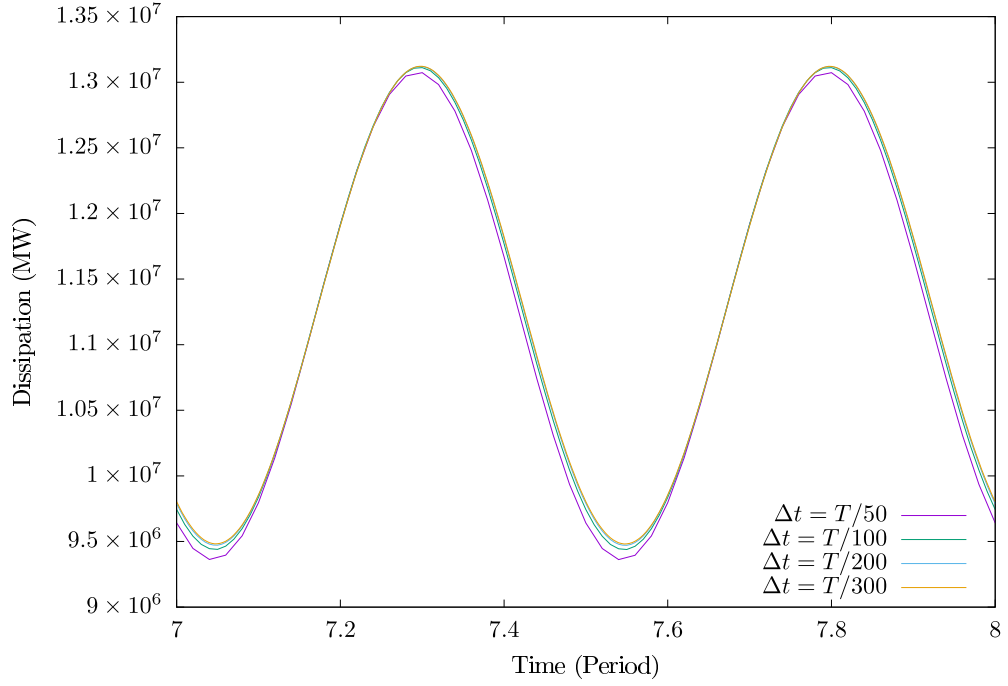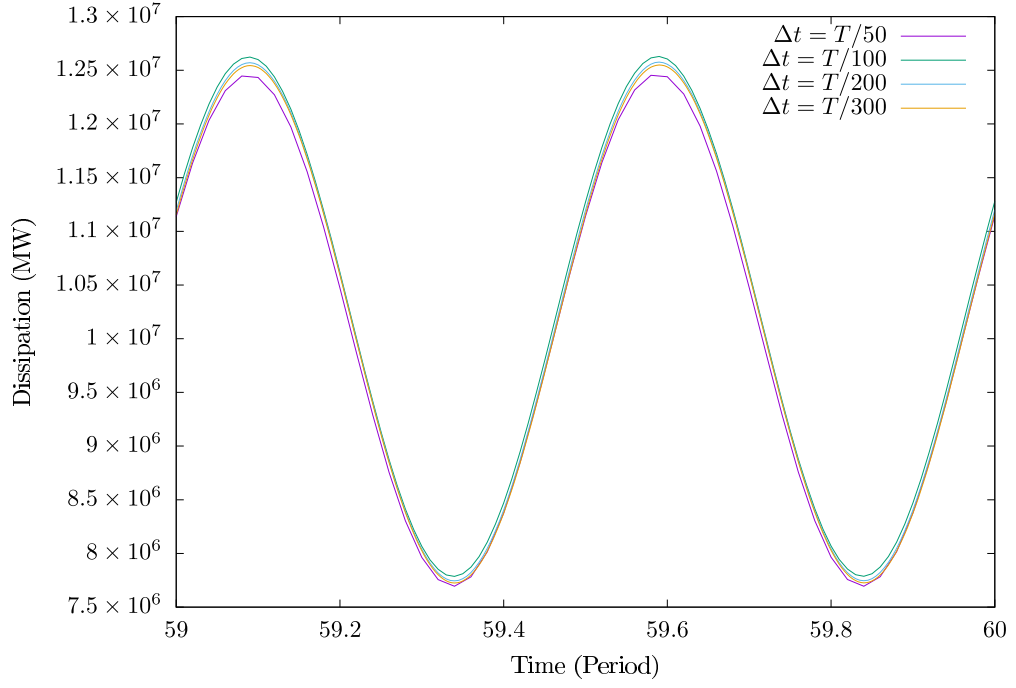
(a) $\eta = 10^6$ Pa·s
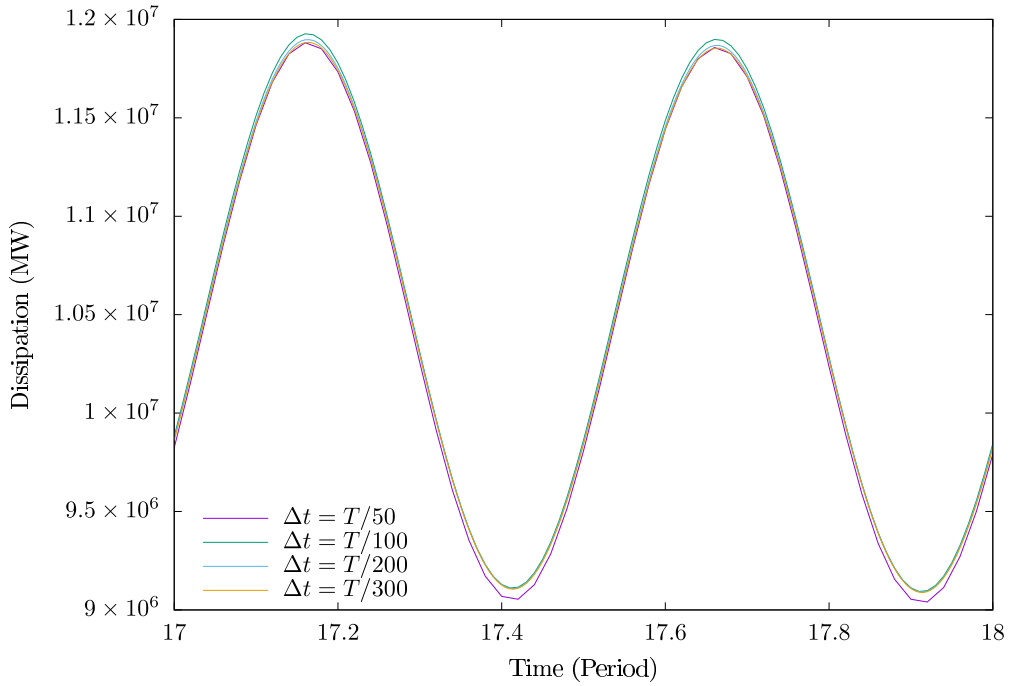
(b) $\eta = 10^5$ Pa·s

Higher values of viscosities can tolerate larger values of time steps, such as $\Delta t = T/100$, see Figure 1.4a, whereas we lose accuracy as viscosity decreases, therefore, we require smaller time steps, for example $\eta = 10^3$ Pa·s requires $\Delta t \leq T/300$. Moreover, smaller viscosities require even smaller time step to ensure the accuracy and stability of the system.
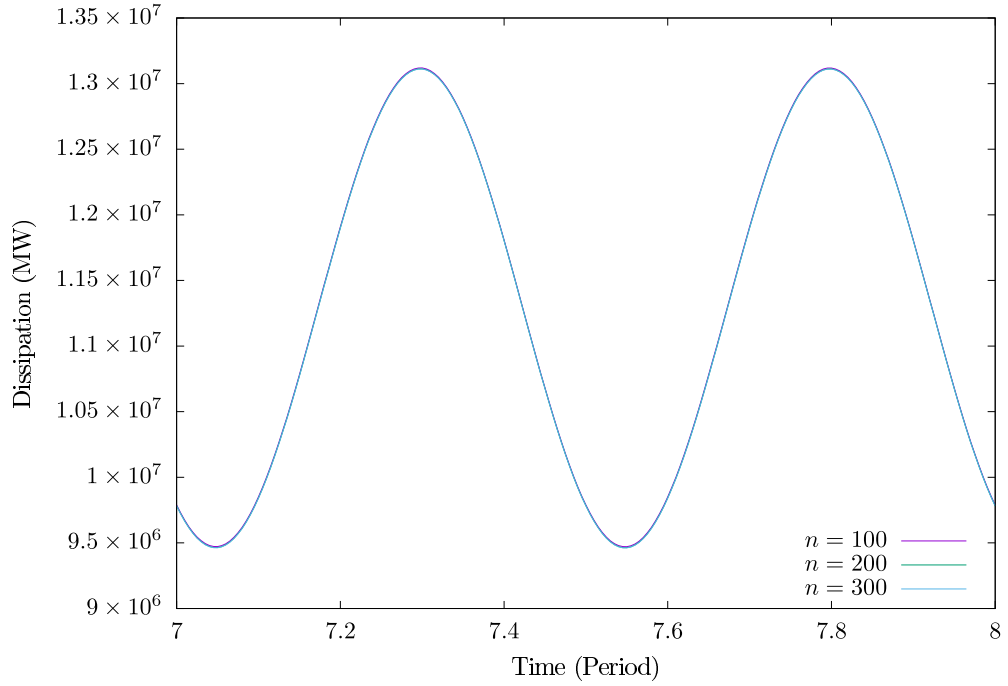
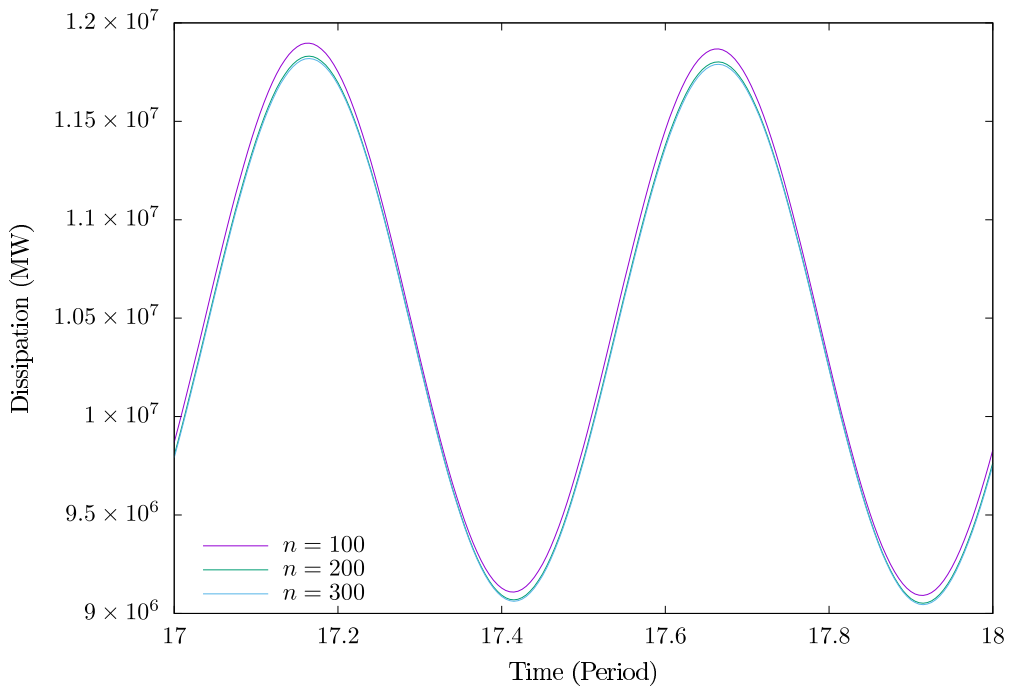(c) $\eta = 10^4$ Pa·s
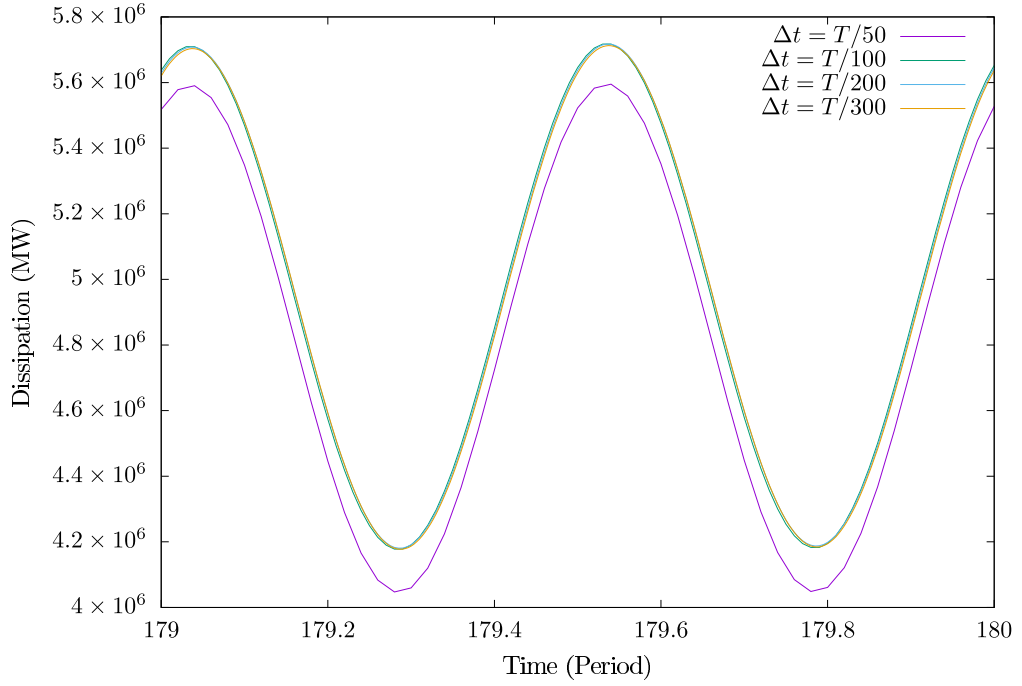
(d) $\eta = 10^3$ Pa·s

Figure 1.4: Convergence of the dissipation curve with respect to time, Δt, for different values of viscosities.

Then to observe the effect of the spatial step size, we fix the time step as constant and compute several radial steps. In Figures 1.5a-1.5d, we plot the
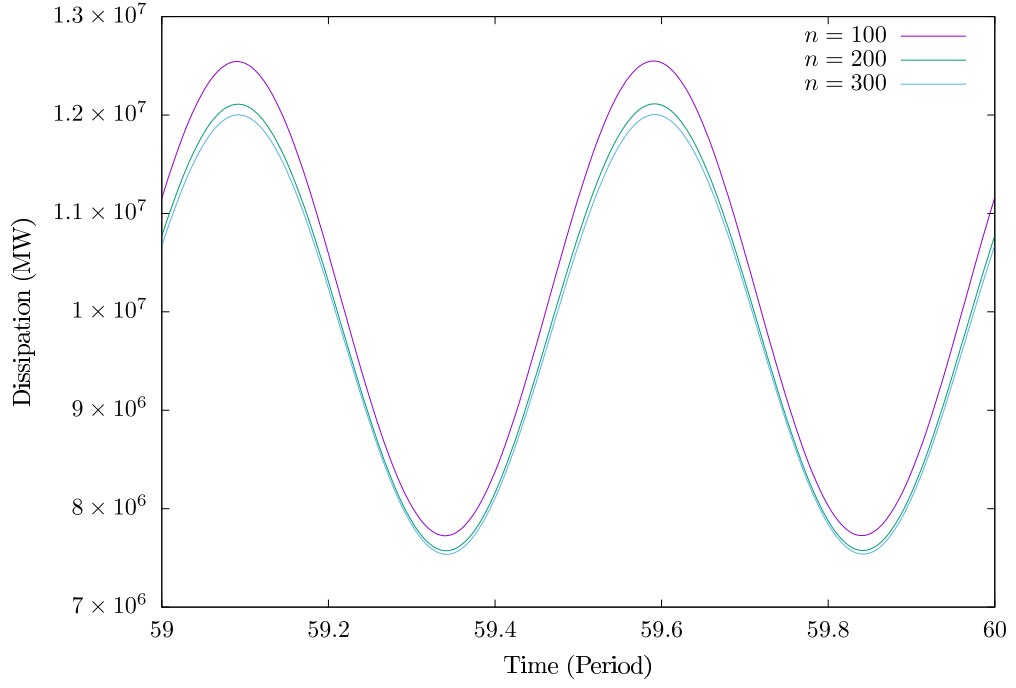
dissipation curves for different number of interfaces, n, which is related to radial step through equation (1.16). We can observe that, higher values of viscosity does not require high number of interfaces, see Figure 1.5a. However, as viscosity gets lower, it is necessary to increase the number of interfaces.
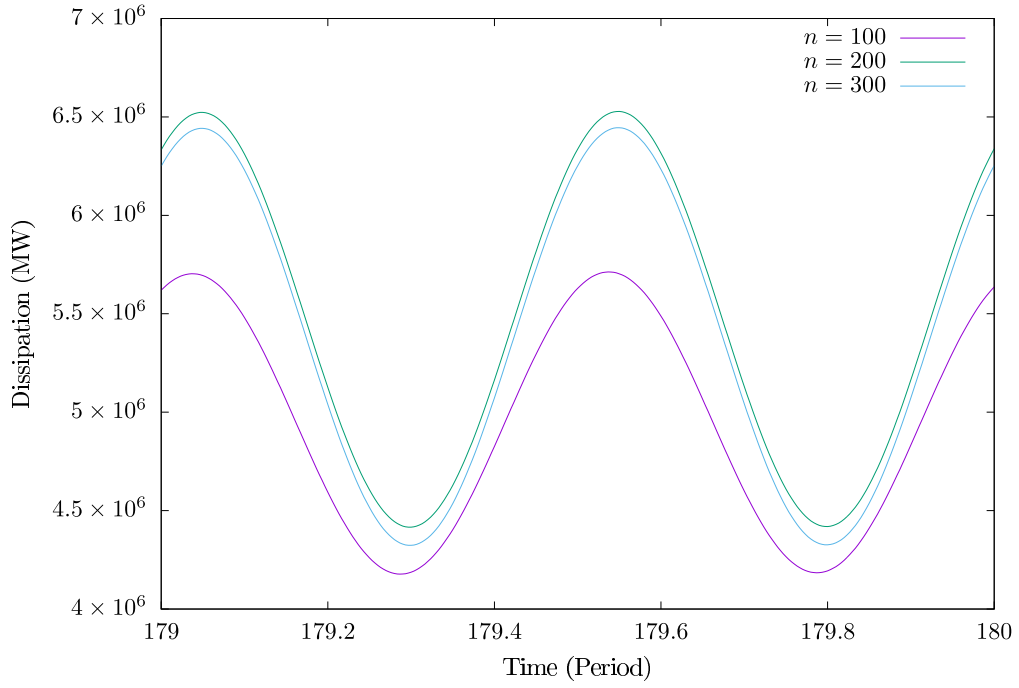

(a) $\eta = 10^6$ Pa·s

(b) $\eta = 10^5$ Pa·s

16

(c) $\eta = 10^4$ Pa·s

(d) $\eta = 10^3$ Pa·s

The analysis of time and spatial step shows us that the method we have prescribed in equation (1.15) is convergent. For the correctness of the computations we investigate the following equation

$$\rho_w \frac{\mathrm{d}}{\mathrm{d}t} \int_{\Omega_w} \boldsymbol{v} \cdot \boldsymbol{v} \mathrm{dx} = \int_{\partial\Omega_w} \mathbb{T}\boldsymbol{n} \cdot \boldsymbol{v} \mathrm{ds} - \int_{\Omega_w} \frac{\mathbb{T}^d : \mathbb{T}^d}{2\eta} \mathrm{dx} + \int_{\Omega_w} \boldsymbol{b} \cdot \boldsymbol{v} \mathrm{dx}, \qquad (1.21)$$

which we compare the right-hand side(RHS) and the left-hand side(LHS) of equa-
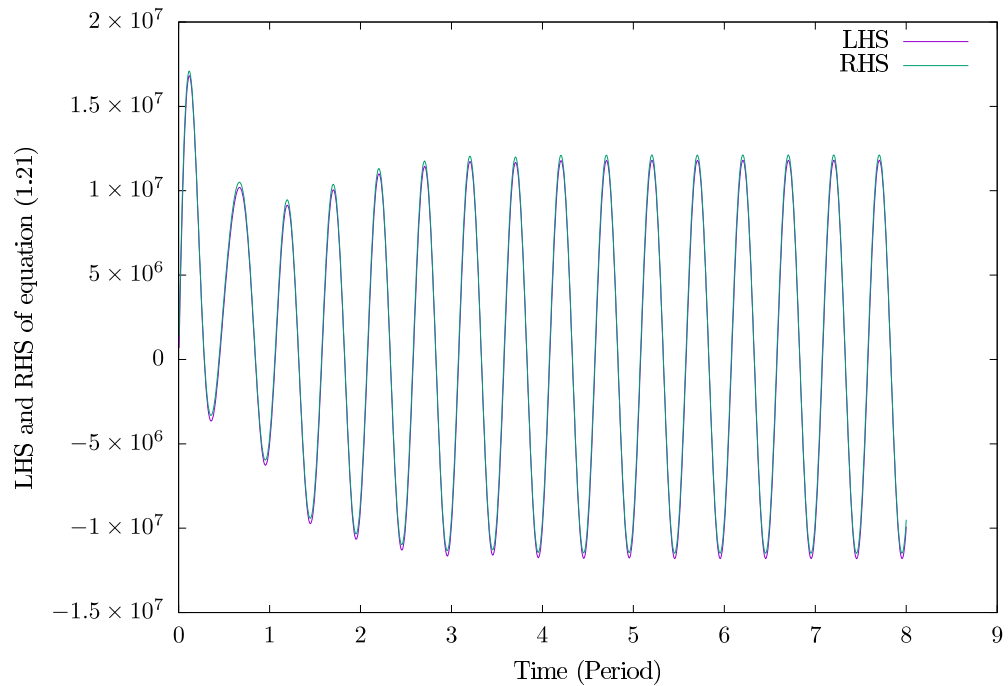
tion (1.21) for viscosity $\eta = 10^6$ Pa·s.

Figure 1.6: The correctness of the method is observed through comparing LHS and RHS of the (1.21).

As we can see from Figure 1.6, for each time instant, the method proposed in this thesis yields an accurate and correct solution. Lastly, for each of the viscosities, we investigate the number of cut-off degree necessary for the computations. Cut-off degree is chosen in such way that the magnitude of dissipation drops approximately by two orders of magnitude. For higher viscosities, a low resolution on spectrum can capture this accuracy, e.g. see Figure 1.7a. However, as viscosity decreases, number of degrees required to obtain the same accuracy increases, see Figures 1.7b-1.7d.
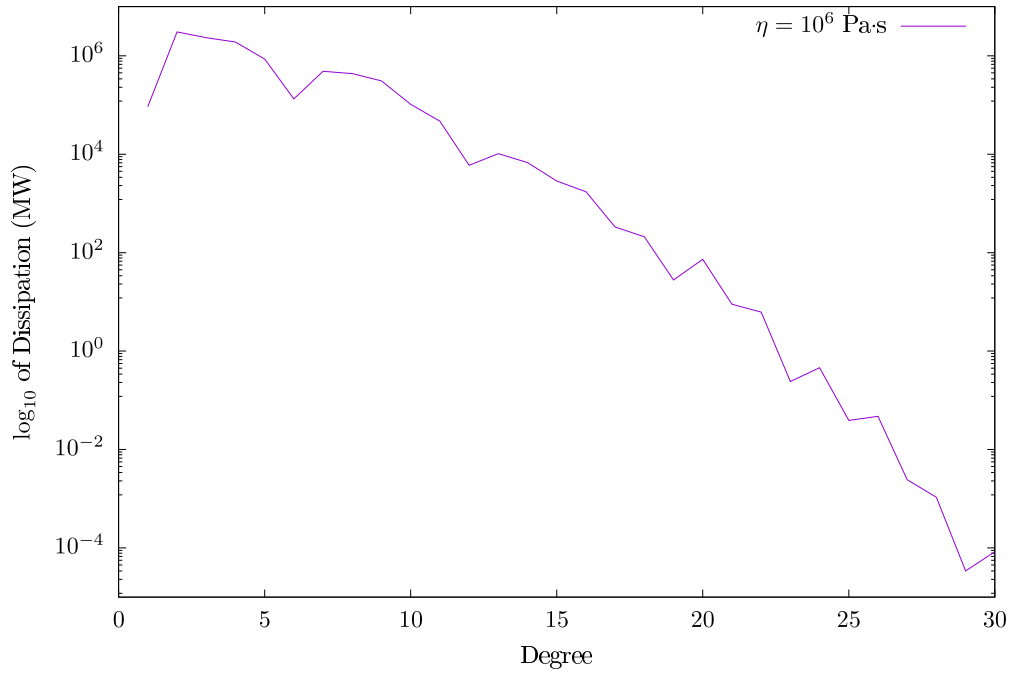
(a) $\eta = 10^6$ Pa·s
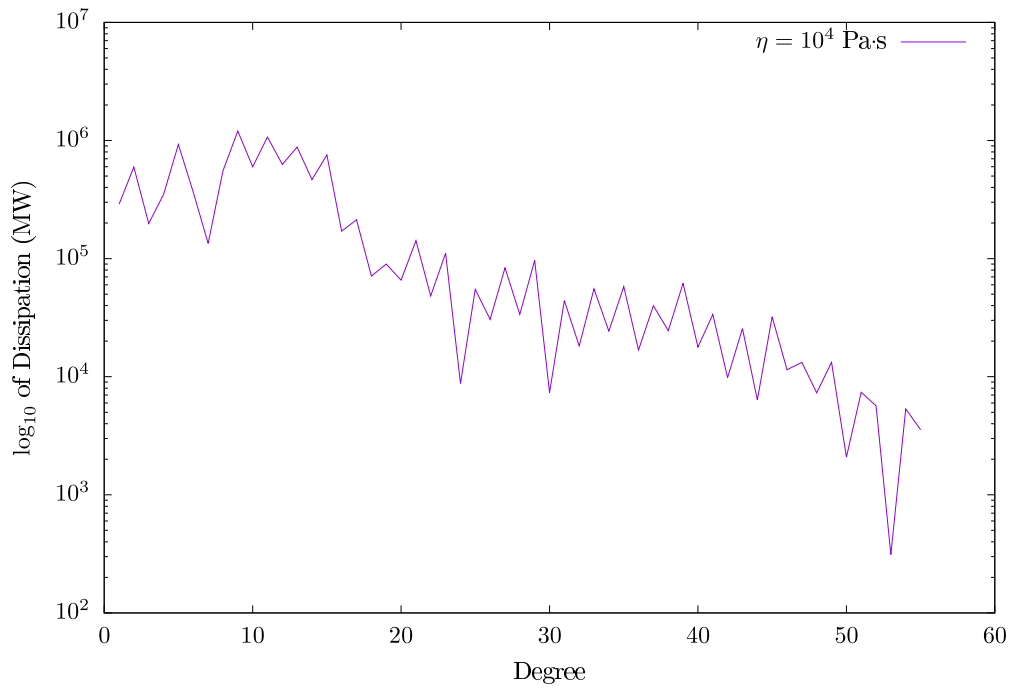
(b) $\eta = 10^5$ Pa·s
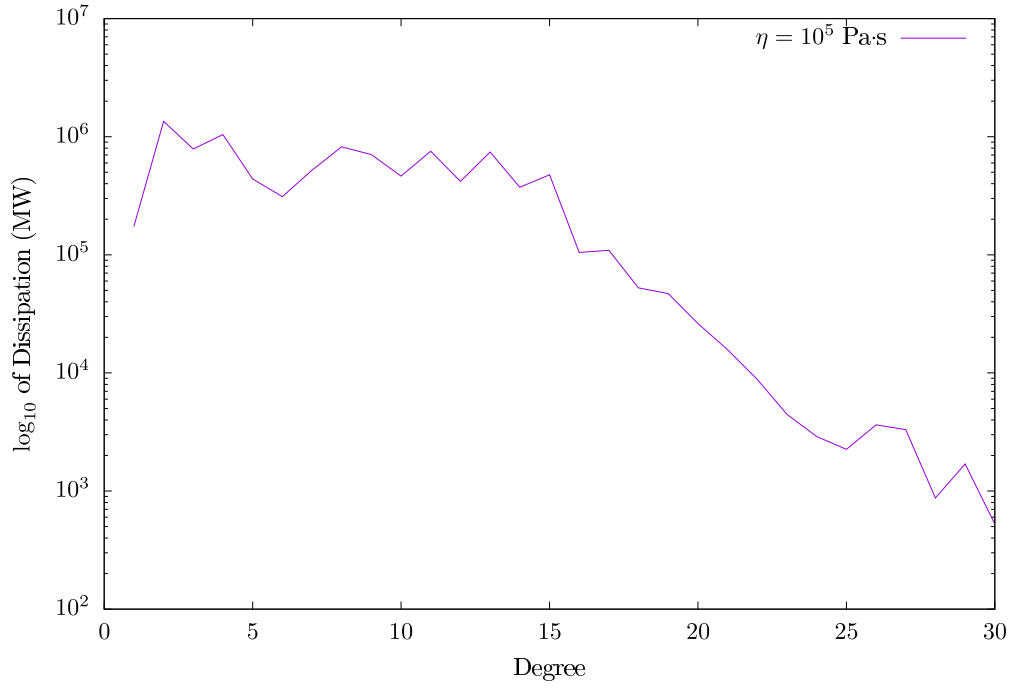
(c) $\eta = 10^4$ Pa·s
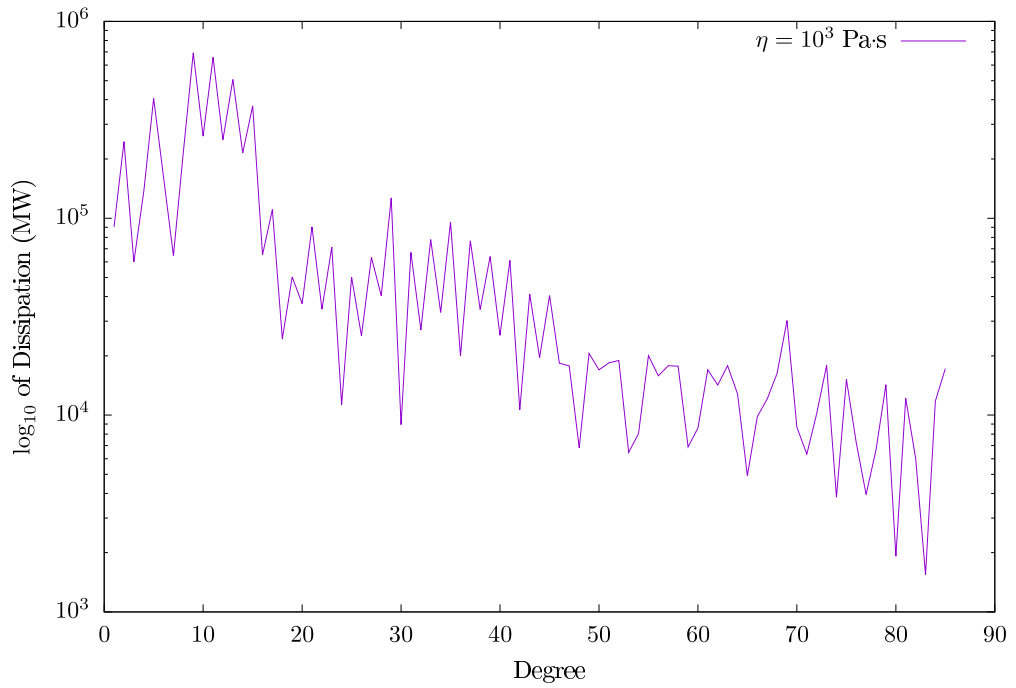
(d) $\eta = 10^3$ Pa·s

Figure 1.7: Spectrum for different values of viscosities

For even lower viscosities, the spectrum increases dramatically. For example, it is estimated that for $\eta = 1$ Pa·s, we require cut-off degree to be approximately 1000.

As mentioned in the beginning of this section, we observed that higher values of viscosity, $\eta = 10^6$ Pa·s, admits lower resolutions, where $\Delta t \leq T/100$, $n \geq 100$ and cut-off degree equals 15 yields an accurate solution within short number of periods. However, we observe that as viscosity becomes $\eta = 10^3$ Pa·s, we require $\Delta t \leq T/300$, $n \geq 300$ and cut-off degree approximately equals to 85, and greater number of periods to reach the accurate steady solution.

2. Results

2.1 Tidal Dissipation

The main focus of this work is to present the tidal dissipation within the ocean of Enceladus. The dissipation produced due to tidal force in the ocean depends on the viscosity and the thickness of the ocean, which we will denote as d. For different values of ocean thicknesses, we investigate the behaviour of the dissipation value as viscosity varies between $\eta = 10^6$-10^3 Pa·s. Depending on the ocean thickness, the dissipation value can increase or decrease as viscosity decreases. If the dissipation value is increasing with decreasing viscosity, we say that the system is in resonance state. Otherwise, we say that the system is in non resonant state.

For high values of $d > 86$ km, the amplitudes of dissipation are smooth with respect to d, and they decrease as the value of the viscosity decreases, see Figure 2.1. It is estimated that, as viscosity approaches to its realistic value, the dissipation will continue decrease for high thicknesses. However, for lower values of d, the behaviour of the system gets complicated. We start to observe some resonance peaks for some values of d, as viscosity decreases. We observe that on the neighborhood of $d = 70$ km and $d = 40$ km the dissipation value increases with decreasing viscosity. This would indicate that as viscosity approaches to $\eta = 10^{-3}$ Pa·s, the dissipation value can increase several orders of magnitude if the resonance state would be attained. Moreover, we can see that as viscosity decreases, more spikes start to appear on the curves.
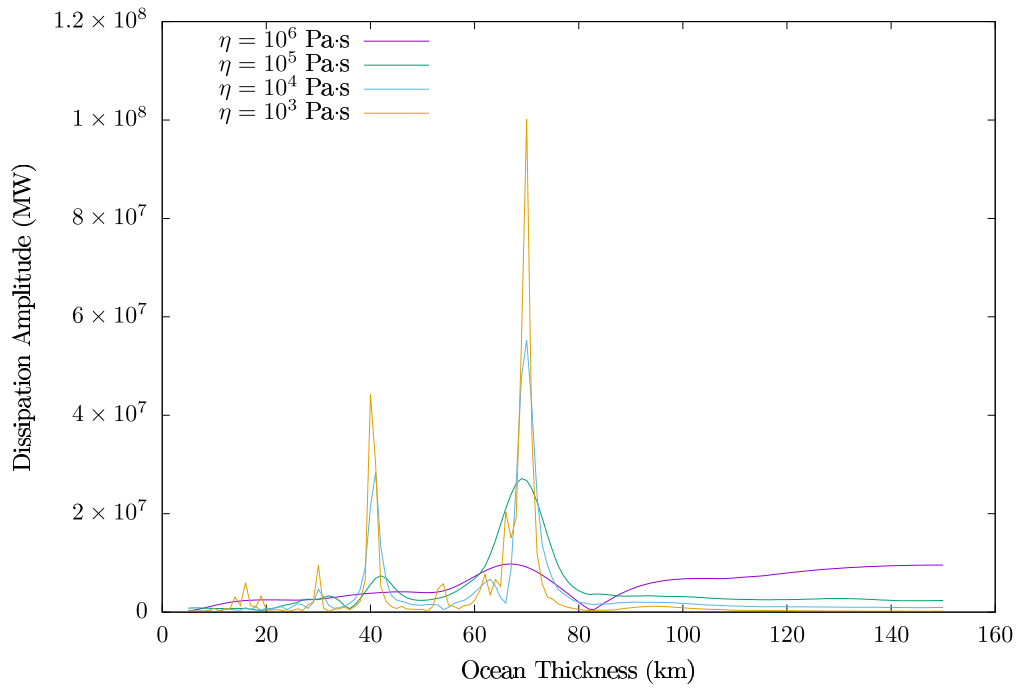
Figure 2.1: Dissipation amplitude depending on the ocean thickness.
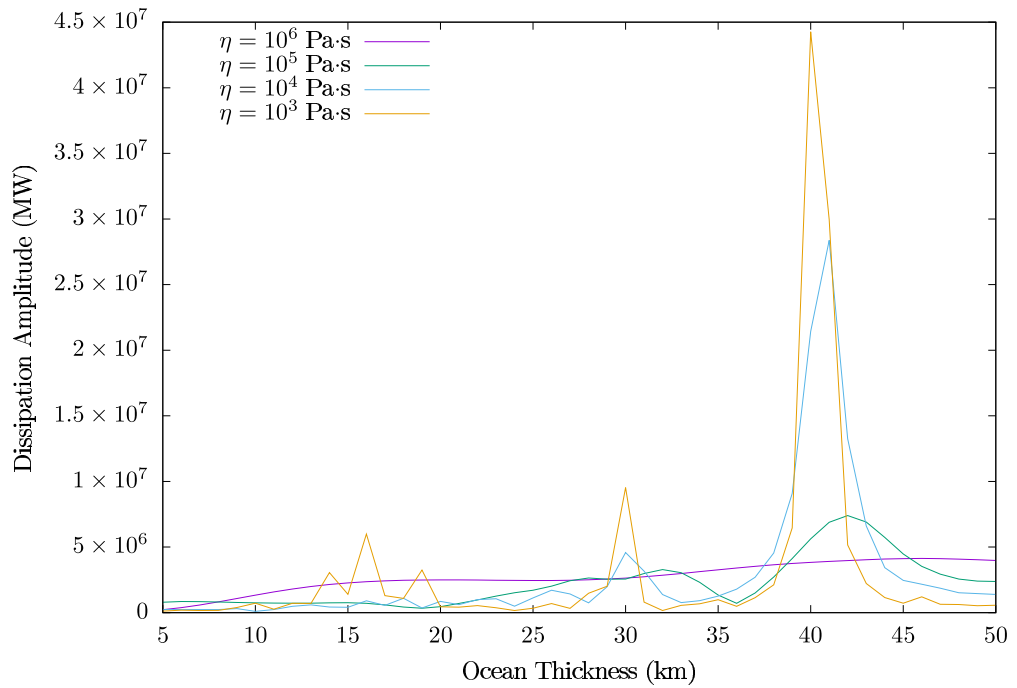

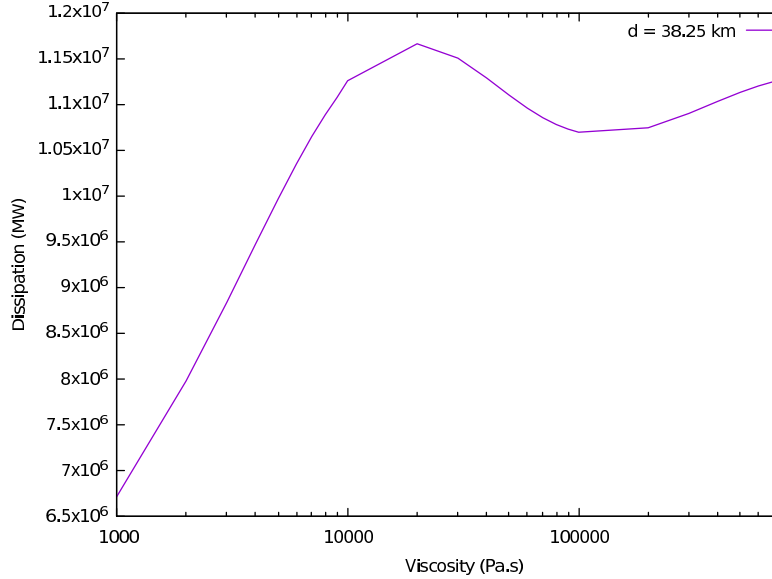Figure 2.2: Zoomed in version of Figure 2.1, between 5 km and 50 km.

Figure 2.3: The dissipation depending on viscosity computed for 38.25 km thick ocean.

We can see from Figure 2.3, for thickness $d = 38.25$ km, the dissipation starts increasing from $\eta = 2\times10^5$ Pa·s and then reaches its maximum around $\eta = 2\times10^4$ Pa·s, and then starts decreasing again. With decreasing viscosity the dissipation begins to decrease, which means $d = 38.25$ km is no longer in the resonance neighborhood. This due to, the resonance neighborhood gets narrow with decreasing viscosity, which makes $d = 38.25$ km to fall out of the neighborhood. This can be also observed from Figure 2.2, where the width of the peaks gets narrow. If the precise value of d is not chosen in the resonance neighborhood, then the dissipation value is going to decrease with decreasing viscosity. In order to capture the precise values of resonance, we would need lower resolution on thickness, where current computations are done for resolution of 1000 m.

2.2 Distribution of Tidal Dissipation

Lastly, we would like to investigate the spatial distribution of the tidal heat flux, which is defined as

$$q\left(\theta, \phi\right) := \frac{1}{T} \int_{T_f-T}^{T_f} \left(\frac{1}{r_t^2} \int_{r_b}^{r_t} \frac{\mathbb{T}^d : \mathbb{T}^d}{2\eta} r^2 \mathrm{d}r \right) \mathrm{d}t, \tag{2.1}$$

where the dissipation is averaged over radius and time. The averaging is particularly important for determining where the tidal heating occurs in ocean. The

24

distribution of the heat flux depends on the thickness of the ocean, as well as the viscosity of water. For thin ocean, e.g. $d = 2$ km, we observe that the heat flux is distributed in wide area for high viscosities, Figures 2.4a and 2.4b. As viscosity continues to decrease, we see that, for thin ocean the heat flux concentrates latitudes 30°, Figures 2.4c and 2.4d. For thin ocean, the maximum value of the heat flux increasing with decreasing viscosity, where it reaches approximately 18 Wm^{-2} for $\eta = 10^3$ Pa·s. The maximum value of the tidal heat flux increases with the decreasing viscosity. However, at the same time the area where the heat flux occurs the most gets smaller. This behaviour can be seen in each thickness that we observe. We can observe heat flux tends to polar regions of the icy moon, with decreasing viscosity, for thicknesses greater than 10 km, Figures 2.5, 2.6, 2.7.
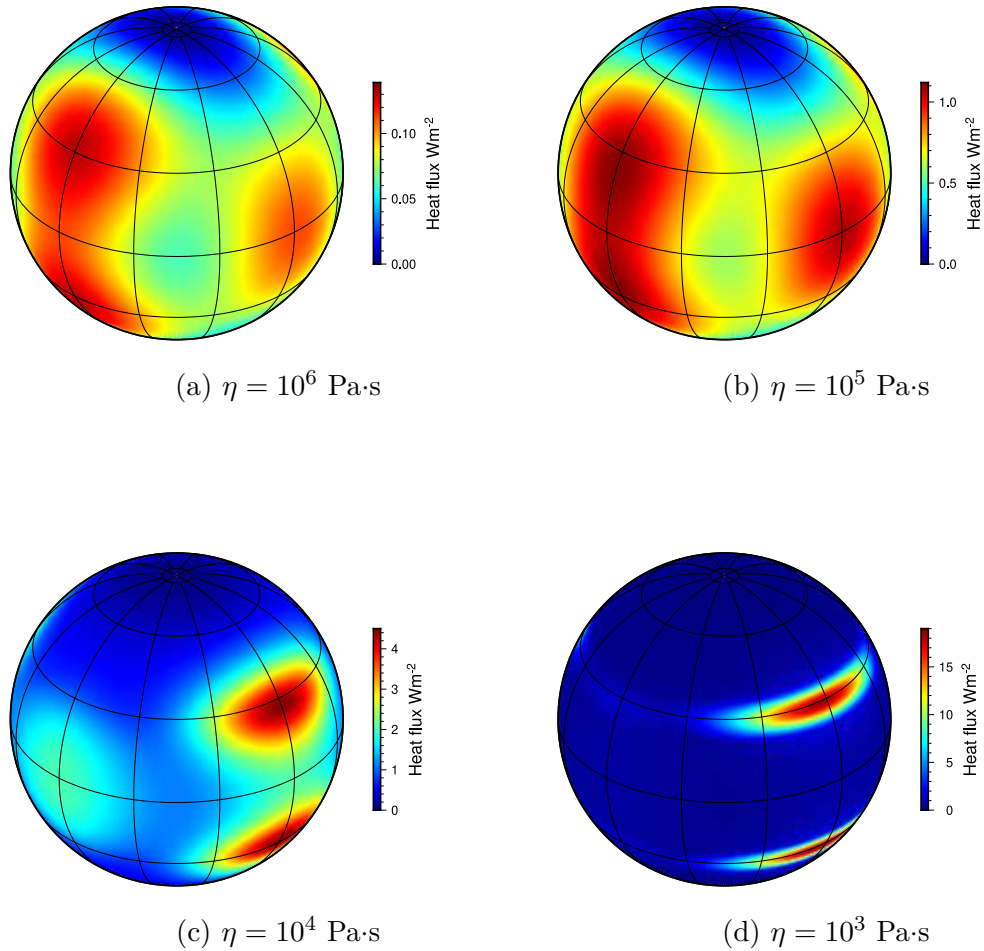

(a) $\eta = 10^6$ Pa·s

(b) $\eta = 10^5$ Pa·s

(c) $\eta = 10^4$ Pa·s

(d) $\eta = 10^3$ Pa·s

Figure 2.4: Spatial distribution of tidal heat flux for $d = 2$ km.

(a) $\eta = 10^6$ Pa·s

(b) $\eta = 10^5$ Pa·s
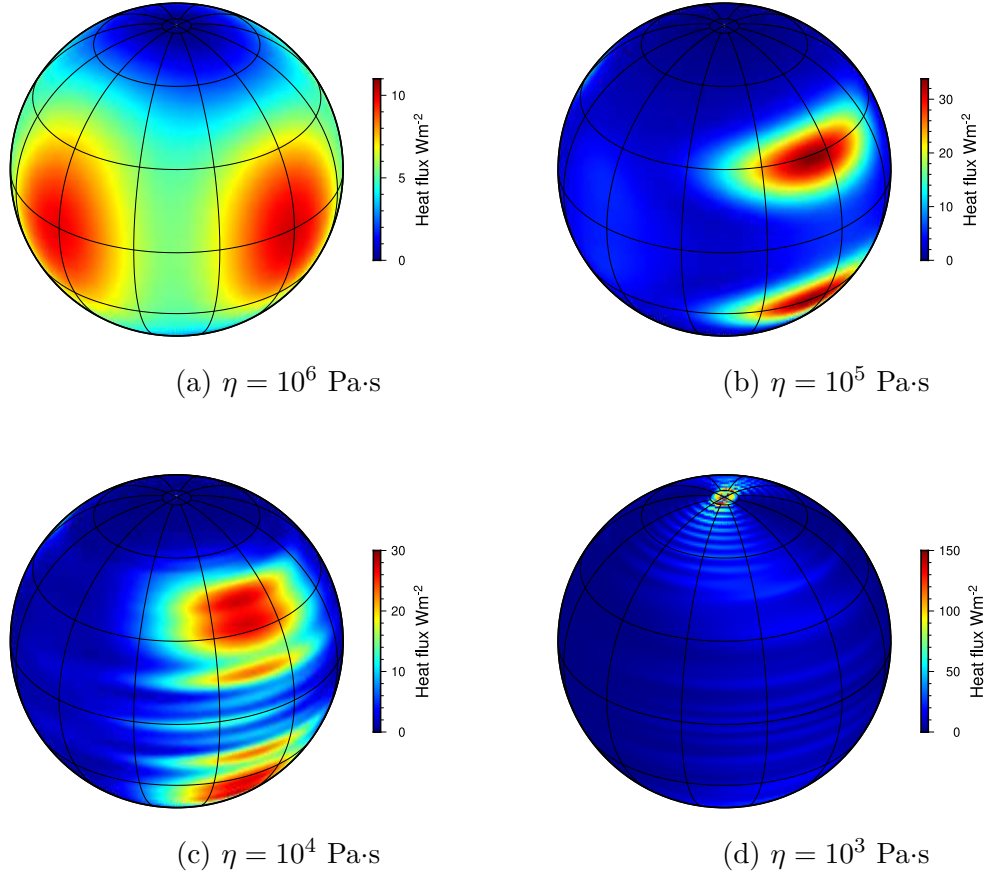
(c) $\eta = 10^4$ Pa·s

(d) $\eta = 10^3$ Pa·s

Figure 2.5: Spatial distribution of tidal heat flux for $d = 10$ km.

For $d = 10$ km, the area where the heat flux is dense, dramatically reduces from $\eta = 10^4$ Pa·s to $\eta = 10^3$ Pa·s, while the maximum value of the heat flux increases by order of one, Figures 2.5c and 2.5d. Moreover, if we compare the Figure 2.2 and the heat flux patterns, for $d = 10$ km and $d = 30$ km, we can see that whenever the resonance peak occurs, the heat flux becomes dense the polar regions, and the area of the heat flux pattern gets smaller, Figures 2.5d and 2.7d. On the other hand, where there is no peak, e.g. $d = 20$ km, the distribution and the maximum value of the heat flux stays the same, Figure 2.6.

(a) $\eta = 10^6$ Pa·s

(b) $\eta = 10^5$ Pa·s

(c) $\eta = 10^4$ Pa·s

(d) $\eta = 10^3$ Pa·s
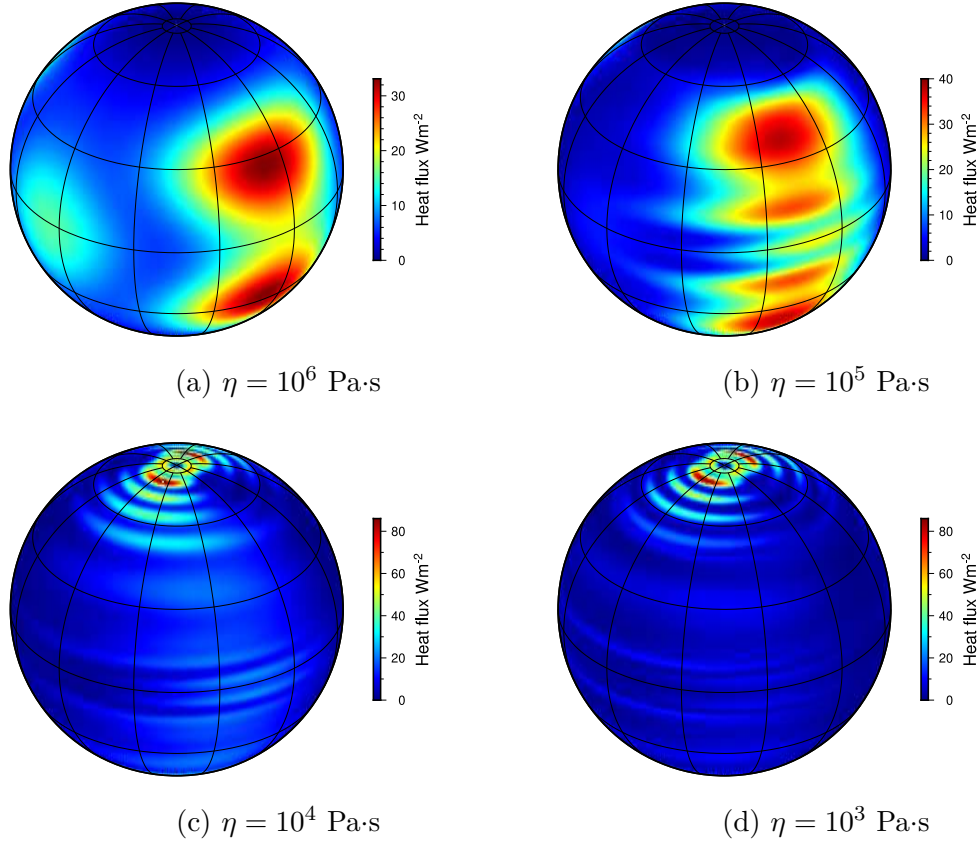
Figure 2.6: Spatial distribution of tidal heat flux for $d = 20$ km.

For 30 km thick ocean, Figure 2.7, when resonant peak occurs, the increase of the heat flux becomes steep and the it goes several order bigger than the observed value. Even for non-resonant thickness, $d = 50$km, where there is no peak, the heat flux concentrates on polar regions of the moon with decreasing viscosity, Figure 2.8. For this case, however, we can observe that the maximum value of the heat flux is decreasing for lower viscosities. It can be estimated that for realistic value of the viscosity, the magnitude of the heat flux will drop significantly at the non resonant states.

(a) $\eta = 10^6$ Pa·s

(b) $\eta = 10^5$ Pa·s

(c) $\eta = 10^4$ Pa·s

(d) $\eta = 10^3$ Pa·s
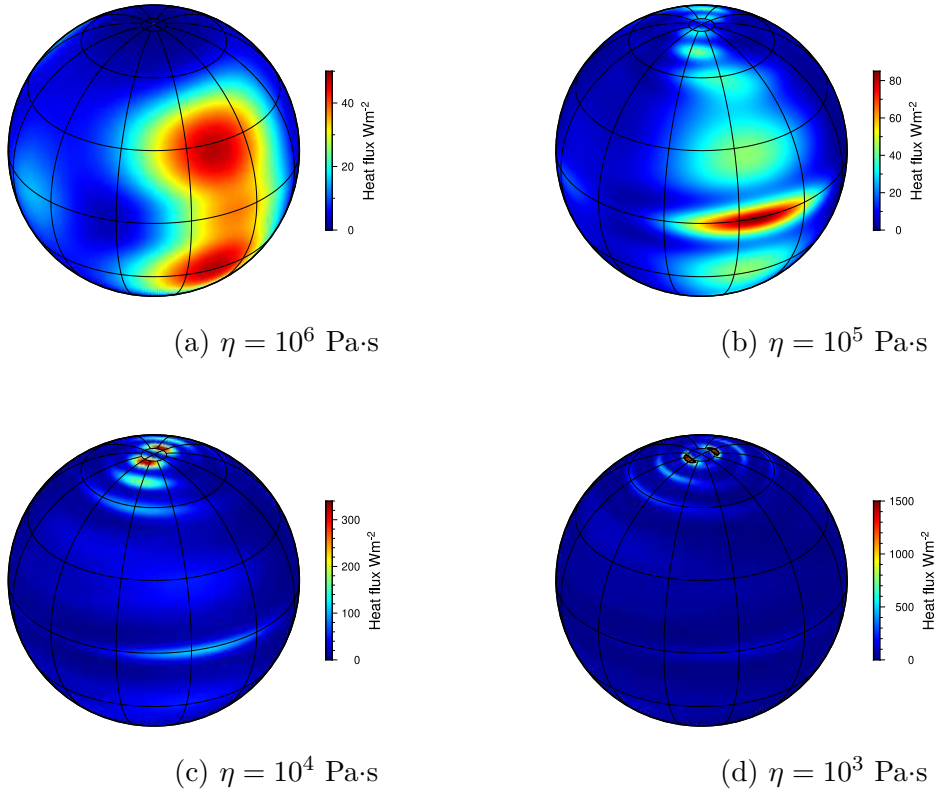
Figure 2.7: Spatial distribution of tidal heat flux for $d = 30$ km.

(a) $\eta = 10^6$ Pa·s

(b) $\eta = 10^5$ Pa·s

(c) $\eta = 10^4$ Pa·s

(d) $\eta = 10^3$ Pa·s
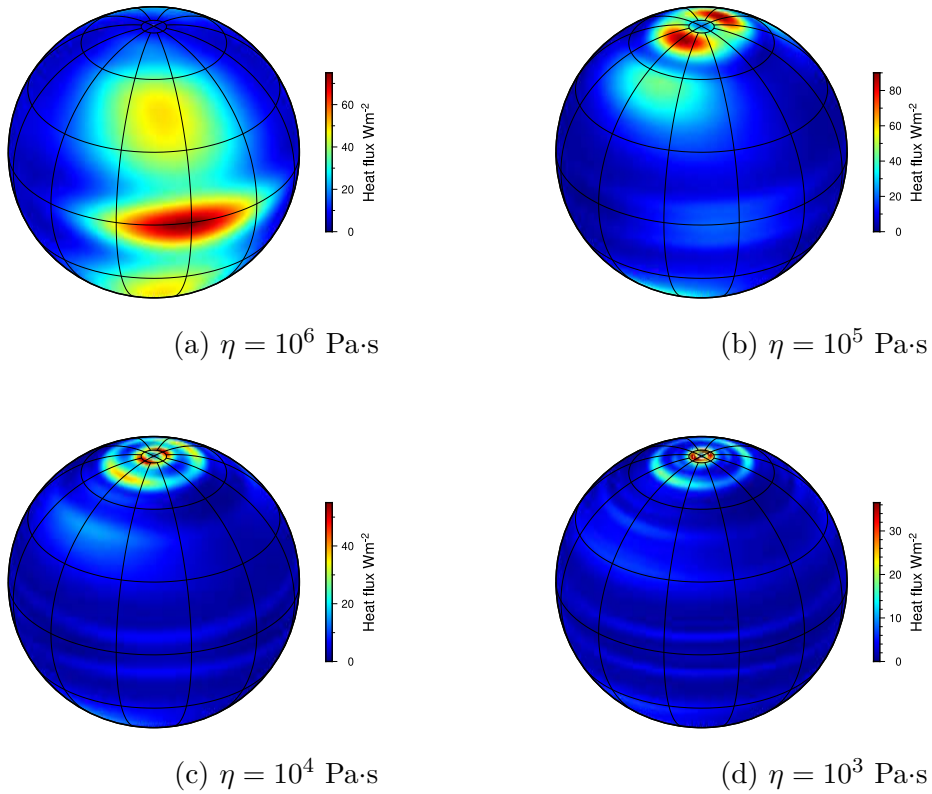
Figure 2.8: Spatial distribution of tidal heat flux for $d = 50$ km.

3. Discussion

The results presented above are consistent with the results from Rovira-Navarro et al. (2019), who carry out the computations in the frequency domain and without the effect of the ice shell. We impose the effect of the ice shell through the top boundary of the ocean and carry out the computations in the time domain. In this new setting, we show that we are able to obtain resonance peaks similar to the ones presented in Rovira-Navarro et al. (2019). The frequency domain and time domain computations behave in a similar way. The dissipation displays spiky behaviour for thinner oceans, whereas for thick oceans the dissipation decreases with decreasing viscosity. Moreover, for given values of viscosities, the magnitude of dissipation we obtain is greater than what they find out. However, the minimum viscosity that we can reach in current computations is $\eta = 10^3$ Pa·s.

In Chen et al. (2014) and Matsuyama et al. (2018), it is proposed that, the tidal heating is not sufficient to heat the icy moons. The approximations from the shallow water equations presents insufficient tidal dissipation to explain the heat observed in Enceladus. In the paper by Matsuyama (2014), it is concluded that the tidal dissipation would be able to compensate the total heat budget provided that the ocean is thin, $d \leq 10$ km. Moreover, in three dimensional calculations, Rovira-Navarro et al. (2019) concluded that the tidal heating would not be enough to keep the ocean in a liquid state. However, the dissipation we obtain, is several orders higher than the ones computed in Rovira-Navarro et al. (2019) and shallow water approximations. Although, we are unable to reach the realistic value of the viscosity of the water, this increase in the dissipation might suggest that, tidal heating can explain the observed values if the resonant state occurs for some thicknesses of the ocean.

In our general setting, there might be resonant peaks for the realistic value of the viscosity, where high values of dissipation can be observed. It is evident that for the high values of viscosity, there are cases where the dissipation is about $\sim 10^4$ GW, e.g. $d = 40$ km and $d = 70$ km. Even though $d = 70$ km is too thick for representing the ocean on Enceladus, $d = 40$ km is close to the value of the realistic thickness of the ocean, when it is assumed that the moon has spherical

geometry. Therefore if the resonant state occurs for in the neighbourhood of $d = 38$ km, there might be enough dissipation produced by the ocean to keep the ocean liquid and explain the total heat observed in Howett et al. (2011).

In the ice shell, it is estimated that the heat flux is concentrated on south pole of the moon (Souček et al., 2019). However, paper by Matsuyama et al. (2018) estimated that the distribution of the heat flux in the ocean is different than the distribution in the ice shell. In that paper, it is found that the heat flux occurs on area around the equator. The distribution of the tidal heat flux depends on the thicknesses for high values of viscosity. The heat flux in thinner oceans spreads large area around the equator. These results show different behaviour when compared with results from paper by Matsuyama et al. (2018), where they found similar the heat flux distribution but for thicker ocean. For greater values of thicknesses, with high viscosity, the tidal heat flux distribution changes between equator and slightly higher degrees of longitudes. With decreasing viscosity the heat flux moves to the poles, for all thicknesses given except for very thin oceans, e.g. $d = 2$ km. Since the heat flux in the ice shell appears on the poles, in particular at the south pole (Souček et al., 2019), the tidal heating in ocean could significantly contribute to the dissipation in ice shell for lower values of viscosity.

The value of globally averaged heat flux is estimated from Howett et al. (2011) as 20 ± 4 mWm^{-2}. For viscosities several order higher than the realistic value of viscosity, we see that the tidal heat flux can easily produce enough heat flux to compensate the observed value. In Matsuyama (2014), it is estimated that the eccentricity tides can produce the observed value of the heat flux, provided that the ocean is thin. Our results, given in Figure 2.4, are consistent with this conclusion. The thin ocean can produce enough heat flux to compensate the observed value. Moreover, we observe that for the given viscosities and ocean thicknesses, the maximum heat flux is above the observed values. The thicknesses $d = 30$ km and $d = 10$ km represents the resonant peaks for the ocean. For these thicknesses, we observe that the heat flux increases unrealistically. For non resonant thickness, e.g. $d = 50$ km, the heat flux has lower values, which could indicate that if resonant state is not attained, the maximum value of the heat flux

could decrease several orders of magnitude as viscosity approaches to $\eta = 10^{-3}$ Pa·s.

Conclusion

In this thesis, we address to problem of tidal dissipation in icy moons. In particular, we choose Enceladus to be our basis model. In order to address this problem, we write the general balance laws and make simplifications, so that the system becomes linear. We consider the effect of the Coriolis force and the ice shell, just within the top boundary. In order to find the dissipation, we employ the spectral method and reduce the equations such that they would depend on time and radius. Then, we solve the equations using the method described in Section 1.4 and Section 1.3. In order to implement these methods, we write a Fortran 90 code and test it for convergence and accuracy in Section 1.5. Then we present the results of the tidal dissipation on Enceladus and discuss these results in the discussion section. We conclude that the dissipation behaviour is similar to Rovira-Navarro et al. (2019) and the system behaves in analogically when we include the time domain. The dissipation depends heavily on viscosity and ocean thickness. Moreover, the dissipation that we find is several orders higher than the previous works estimated. Therefore, tidal potential still has an important role in heating Enceladus. However, we made several assumptions that can be improved. Firstly, we omitted the non-linear turbulent term ($\boldsymbol{v} \cdot \nabla \boldsymbol{v}$) in the Navier-Stokes equations. The effect of non-linear term might have important contributions to the heat budget of Enceladus. The method given in the time domain allows us to include the non-linear term in the future calculations. Secondly, we only imposed the effect of the ice shell through top boundary and we assumed that the ice shell is elastic. However, the viscoelastic models of the ice shell could change the dissipation behaviour. We also omitted the effect of the ocean on the ice shell. Finally, we assumed that the ice shell and ocean has constant thickness, but the ice shell and ocean do not have constant thickness; rather, the thickness of the ice shell and ocean varies from the poles to the equator (Čadek et al., 2016; Beuthe et al., 2016). This can lead to different heat flux patterns and change the behaviour on the resonant peaks.

Bibliography

BEUTHE, M., RIVOLDINI, A. AND TRINH, A. (2016). Enceladus's and Dione's floating ice shells supported by minimum stress isostasy. *Geophysical Research Letters*, **43**(19), 10,088–10,096.

CHEN, E. AND NIMMO, F. (2011). Obliquity tides do not significantly heat Enceladus. *Icarus*, **214**(2), 779 – 781. ISSN 0019-1035.

CHEN, E., NIMMO, F. AND GLATZMAIER, G. (2014). Tidal heating in icy satellite oceans. *Icarus*, **229**, 11 – 30. ISSN 0019-1035.

GRIFFITHS, D. F. AND HIGHAM, D. J. (2010). *Numerical methods for ordinary differential equations: initial value problems*. Springer Science & Business Media.

HAY, H. C. AND MATSUYAMA, I. (2019). Nonlinear tidal dissipation in the subsurface oceans of Enceladus and other icy satellites. *Icarus*, **319**, 68 – 85. ISSN 0019-1035.

HOWETT, C. J. A., SPENCER, J. R., PEARL, J. AND SEGURA, M. (2011). High heat flow from Enceladus' south polar region measured using 10-600 cm^{-1} Cassini/CIRS data. *Journal of Geophysical Research: Planets*, **116**(E3).

MÁLEK, J. AND PRŮŠA, V. (2016). *Derivation of Equations for Continuum Mechanics and Thermodynamics of Fluids*, pages 1–70. Springer International Publishing, Cham. ISBN 978-3-319-10151-4.

MATAS, J. (1995). Mantle viscosity and density structure. Master's thesis, Faculty of Mathematics and Physics, Charles University, Prague.

MATSUYAMA, I. (2014). Tidal dissipation in the oceans of icy satellites. *Icarus*, **242**, 11 – 18. ISSN 0019-1035.

MATSUYAMA, I., BEUTHE, M., HAY, H. C., NIMMO, F. AND KAMATA, S. (2018). Ocean tidal heating in icy satellites with solid shells. *Icarus*, **312**, 208 – 230. ISSN 0019-1035.

NIMMO, F. AND PAPPALARDO, R. T. (2016). Ocean worlds in the outer solar system. *Journal of Geophysical Research: Planets*, **121**(8), 1378 – 1399.

NIMMO, F., BARR, A. C., BĚHOUNKOVÁ, M. AND MCKINNON, W. B. (2018). *Enceladus and the Icy Moons of Saturn*, chapter The Thermal and Orbital Evolution of Enceladus: Observational Constraints and Models, page 79. University of Arizona Press.

PORCO, C. C., HELFENSTEIN, P., THOMAS, P. C., INGERSOLL, A. P., WISDOM, J., WEST, R., NEUKUM, G., DENK, T., WAGNER, R., ROATSCH, T., KIEFFER, S., TURTLE, E., MCEWEN, A., JOHNSON, T. V., RATHBUN, J., VEVERKA, J., WILSON, D., PERRY, J., SPITALE, J., BRAHIC, A., BURNS, J. A., DELGENIO, A. D., DONES, L., MURRAY, C. D. AND SQUYRES, S. (2006). Cassini Observes the Active South Pole of Enceladus. *Science*, **311** (5766), 1393–1401. ISSN 0036-8075.

ROVIRA-NAVARRO, M., RIEUTORD, M., GERKEMA, T., MAAS, L. R., VAN DER WAL, W. AND VERMEERSEN, B. (2019). Do tidally-generated inertial waves heat the subsurface oceans of Europa and Enceladus? *Icarus*, **321**, 126 – 140. ISSN 0019-1035.

SOUČEK, O., HRON, J., BĚHOUNKOVÁ, M. AND ČADEK, O. (2016). Effect of the tiger stripes on the deformation of Saturn's moon Enceladus. *Geophysical Research Letters*, **43**(14), 7417–7423.

SOUČEK, O., BĚHOUNKOVÁ, M., ČADEK, O., HRON, J., TOBIE, G. AND CHOBLET, G. (2019). Tidal dissipation in Enceladus' uneven, fractured ice shell. *Icarus*, **328**, 218 – 231. ISSN 0019-1035.

THOMAS, P., TAJEDDINE, R., TISCARENO, M., BURNS, J., JOSEPH, J., LOREDO, T., HELFENSTEIN, P. AND PORCO, C. (2016). Enceladus's measured physical libration requires a global subsurface ocean. *Icarus*, **264**, 37 – 47. ISSN 0019-1035.

VALLIS, G. K. (2017). *Atmospheric and Oceanic Fluid Dynamics: Fundamentals and Large-Scale Circulation*. Cambridge University Press, 2 edition.

Varshalovich, D. A., Moskalev, A. N. and Khersonskii, V. K. (1988). *Quantum Theory of Angular Momentum.* WORLD SCIENTIFIC.

Čadek, O., Tobie, G., Van Hoolst, T., Massé, M., Choblet, G., Lefèvre, A., Mitri, G., Baland, R.-M., Běhounková, M., Bourgeois, O. and Trinh, A. (2016). Enceladus's internal ocean and ice shell constrained from Cassini gravity, shape, and libration data. *Geophysical Research Letters,* **43**(11), 5653–5660.

List of Figures

List of Tables

List of Abbreviations

A. Appendix

In this appendix, we summarize basic properties of spherical harmonics. We use the spherical harmonics to reduce the partial differential equations to ordinary differential equations.

A.1 Functions in terms of Spherical Harmonics

Spherical harmonics forms an orthonormal basis for scalar, vector and tensor functions that are square integrable, i.e. $L^2(S)$, where S is the unit sphere (Matas, 1995, Varshalovich et al., 1988). Therefore, functions $f(r,\theta,\phi), \boldsymbol{f}(r,\theta,\phi)$ and $\mathbb{F}(r,\theta,\phi)$ can be written as linear combination of the spherical harmonics as,

$$f(r,\theta,\phi) = \sum_{j=0}^{\infty} \sum_{m=-j}^{j} f_{jm}(r) Y_{jm}(\theta,\phi), \tag{A.1}$$

$$\boldsymbol{f}(r,\theta,\phi) = \sum_{j=0}^{\infty} \sum_{m=-j}^{j} \sum_{l=j-1}^{j+1} f_{jm}^l(r) \, \boldsymbol{Y}_{jm}^l(\theta,\phi), \tag{A.2}$$

$$\mathbb{F}(r,\theta,\phi) = \sum_{j=0}^{\infty} \sum_{m=-j}^{j} \sum_{l=|j-k|}^{j+k} \sum_{k=0}^{2} F_{jm}^{lk}(r) \, \mathbb{Y}_{jm}^{lk}(\theta,\phi). \tag{A.3}$$

By the orthonormal relations of the spherical harmonics, coefficients $f_{jm}(r)$, $f_{jm}^l(r)$ and $F_{jm}^{lk}(r)$ are given as

$$f_{jm}(r) = \int_0^\pi \int_0^{2\pi} f(r,\theta,\phi) Y_{jm}^*(\theta,\phi) \sin\theta \mathrm{d}\theta \mathrm{d}\phi, \tag{A.4}$$

$$f_{jm}^l(r) = \int_0^\pi \int_0^{2\pi} \boldsymbol{f}(r,\theta,\phi) \cdot \boldsymbol{Y}_{jm}^{l*}(\theta,\phi) \sin\theta \mathrm{d}\theta \mathrm{d}\phi, \tag{A.5}$$

$$F_{jm}^{lk}(r) = \int_0^\pi \int_0^{2\pi} \mathbb{F}(r,\theta,\phi) : \mathbb{Y}_{jm}^{lk*}(\theta,\phi) \sin\theta \mathrm{d}\theta \mathrm{d}\phi, \tag{A.6}$$

where $*$ denotes the complex conjugate of the spherical harmonics.

A.2 Formulas

Formulas that are used in the computations are summarized in this section. Let $\boldsymbol{e}_r$ be the unit vector normal to the surface of the sphere. The functions f, $\boldsymbol{f}$ and

$\mathbb{F}$ have the following forms when multiplied by unit normal vector $\boldsymbol{e}_r$:

$$[f\boldsymbol{e}_r]_{jm}^{j-1} = \sqrt{\frac{j}{2j+1}} f_{jm},$$

$$[f\boldsymbol{e}_r]_{jm}^{j+1} = -\sqrt{\frac{j+1}{2j+1}} f_{jm}, \tag{A.7}$$

$$[\boldsymbol{f} \cdot \boldsymbol{e}_r]_{jm} = \sqrt{\frac{j}{2j+1}} f_{jm}^{j-1} - \sqrt{\frac{j+1}{2j+1}} f_{jm}^{j+1}, \tag{A.8}$$

$$[\mathbb{F}\boldsymbol{e}_r]_{jm}^{j-1} = -\sqrt{\frac{j}{3(2j+1)}} F_{jm}^{j,0} + \sqrt{\frac{j-1}{2j-1}} F_{jm}^{j-2,2} - \sqrt{\frac{(j+1)(2j+3)}{6(2j+1)(2j-1)}} F_{jm}^{j,2}, \tag{A.9}$$

$$[\mathbb{F}\boldsymbol{e}_r]_{jm}^{j} = \sqrt{\frac{j-1}{2(2j+1)}} F_{jm}^{j-1} - \sqrt{\frac{j+2}{2(2j+1)}} F_{jm}^{j+1}, \tag{A.10}$$

$$[\mathbb{F}\boldsymbol{e}_r]_{jm}^{j+1} = \sqrt{\frac{j+1}{3(2j+1)}} F_{jm}^{j,0} - \sqrt{\frac{j+2}{2j+3}} F_{jm}^{j-2,2} + \sqrt{\frac{j(2j-1)}{6(2j+1)(2j+3)}} F_{jm}^{j,2}. \tag{A.11}$$

The cross product between the normal $\boldsymbol{e}_r$ and vector spherical harmonics is used to express the Coriolis force. We give the directly the formula for the Coriolis force given in (1.3b)

$$\boldsymbol{\omega} \times \boldsymbol{v} = (\boldsymbol{f}_c)_{jm}^{l} \boldsymbol{Y}_{jm}^{l}(\theta, \phi), \tag{A.12}$$

where the coefficients are given as

$$(\boldsymbol{f}_c)_{jm}^{l} = \sqrt{6}i \, (-1)^{l+j} \sum_{j_2} v_{j_2m}^{l} \sqrt{2j_2+1}\, C. \tag{A.13}$$

The constant C is given in terms of Clebsh-Gordon coefficients, $C_{j_2m10}^{jm}$, and the 6-j coefficients by (see Matas, 1995 for details)

$$C = C_{j_2m10}^{jm} \begin{Bmatrix} j_2 & 1 & l \\ 1 & j & 1 \end{Bmatrix}. \tag{A.14}$$

We continue the summary of the formulas with the differential operators, such as gradient and divergence. The gradient of scalar function f is given by

$$\nabla f(r, \theta, \phi) = [\nabla f]_{jm}^{j-1} \boldsymbol{Y}_{jm}^{j-1}(\theta, \phi) + [\nabla f]_{jm}^{j+1} \boldsymbol{Y}_{jm}^{j+1}(\theta, \phi), \tag{A.15}$$

where

$$
\begin{aligned}
[\nabla f]_{jm}^{j-1} &= \sqrt{\frac{j}{2j+1}} \left(\frac{\partial f_{jm}}{\partial r} + \frac{j+1}{r} f_{jm} \right), \\
[\nabla f]_{jm}^{j+1} &= -\sqrt{\frac{j+1}{2j+1}} \left(\frac{\partial f_{jm}}{\partial r} - \frac{j}{r} f_{jm} \right).
\end{aligned}
\tag{A.16}
$$

The divergence of vector field $\boldsymbol{f}$ is given by

$$
\operatorname{div} \boldsymbol{f} = [\operatorname{div} \boldsymbol{f}]_{jm} Y_{jm}(\theta, \phi),
\tag{A.17}
$$

where

$$
\begin{aligned}
[\operatorname{div} \boldsymbol{f}]_{jm} &= \sqrt{\frac{j}{2j+1}} \left(\frac{\partial f_{jm}^{j-1}}{\partial r} - \frac{j-1}{r} f_{jm}^{j-1} \right) \\
&\quad - \sqrt{\frac{j+1}{2j+1}} \left(\frac{\partial f_{jm}^{j+1}}{\partial r} + \frac{j+2}{r} f_{jm}^{j+1} \right).
\end{aligned}
\tag{A.18}
$$

The divergence of tensor field $\mathbb{F}$ is given by

$$
\operatorname{div} \mathbb{F}(r, \theta, \phi) = \sum_{l=|j-1|}^{j+1} [\operatorname{div} \mathbb{F}]_{jm}^{l} \, \boldsymbol{Y}_{jm}^{l}(\theta, \phi),
\tag{A.19}
$$

where the coefficients have the following forms

$$
\begin{aligned}
[\operatorname{div} \mathbb{F}]_{jm}^{j-1} &= -\sqrt{\frac{j}{3(2j+1)}} \left(\frac{\partial F_{jm}^{j0}}{\partial r} + \frac{j+1}{r} F_{jm}^{j0} \right) \\
&\quad - \sqrt{\frac{(j+1)(2j+3)}{6(2j-1)(2j+1)}} \left(\frac{\partial F_{jm}^{j,2}}{\partial r} + \frac{j+1}{r} F_{jm}^{j,2} \right) \\
&\quad + \sqrt{\frac{j-1}{2j-1}} \left(\frac{\partial F_{jm}^{j-2,2}}{\partial r} - \frac{j-2}{r} F_{jm}^{j-2,2} \right),
\end{aligned}
\tag{A.20}
$$

$$
\begin{aligned}
[\operatorname{div} \mathbb{F}]_{jm}^{j} &= \sqrt{\frac{j-1}{2j-1}} \left(\frac{\partial F_{jm}^{j-1,2}}{\partial r} - \frac{j-2}{r} F_{jm}^{j-1,2} \right) \\
&\quad - \sqrt{\frac{j+2}{2(2j+1)}} \left(\frac{\partial F_{jm}^{j+1,2}}{\partial r} + \frac{j+2}{r} F_{jm}^{j+1,2} \right),
\end{aligned}
\tag{A.21}
$$

$$
\begin{aligned}
[\operatorname{div} \mathbb{F}]_{jm}^{j+1} &= \sqrt{\frac{j+1}{3(2j+1)}} \left(\frac{\partial F_{jm}^{j0}}{\partial r} - \frac{j}{r} F_{jm}^{j0} \right) \\
&\quad + \sqrt{\frac{j(2j-1)}{6(2j+3)(2j+1)}} \left(\frac{\partial F_{jm}^{j,2}}{\partial r} - \frac{j}{r} F_{jm}^{j,2} \right) \\
&\quad - \sqrt{\frac{j+2}{2j+3}} \left(\frac{\partial F_{jm}^{j+2,2}}{\partial r} + \frac{j+3}{r} F_{jm}^{j+2,2} \right).
\end{aligned}
\tag{A.22}
$$

Let us denote the symmetric part of the $\nabla \boldsymbol{f}$ as $\mathbb{D}_{\boldsymbol{f}} = \frac{1}{2}\left(\nabla \boldsymbol{f} + (\nabla \boldsymbol{f})^T\right)$, then for each $j = 1, 2, \dots$ and $m = -j, \dots, j$, we have

$$\mathbb{D}_{\boldsymbol{f}} = \sum_{l=|j-2|}^{j+2} [\mathbb{D}_{\boldsymbol{f}}]_{jm}^{l,2}\, \mathbb{Y}_{jm}^{l,2}(\theta, \phi). \tag{A.23}$$

Then the coefficients are given as

$$[\mathbb{D}_{\boldsymbol{f}}]_{jm}^{j-2,2} = \sqrt{\frac{j-1}{2j-1}}\left(\frac{\partial f_{jm}^{j-1}}{\partial r} + \frac{j}{r} f_{jm}^{j-1}\right), \tag{A.24}$$

$$[\mathbb{D}_{\boldsymbol{f}}]_{jm}^{j-1,2} = \sqrt{\frac{j-1}{2(2j+1)}}\left(\frac{\partial f_{jm}^{j}}{\partial r} + \frac{j+1}{r} f_{jm}^{j}\right), \tag{A.25}$$

$$[\mathbb{D}_{\boldsymbol{f}}]_{jm}^{j,2} = -\sqrt{\frac{j(j+1)(2j+3)}{6(2j-1)(2j+1)}}\left(\frac{\partial f_{jm}^{j-1}}{\partial r} - \frac{j-1}{r} f_{jm}^{j-1}\right)$$
$$+ \sqrt{\frac{j(2j-1)}{6(2j+3)(2j+1)}}\left(\frac{\partial f_{jm}^{j+1}}{\partial r} + \frac{j+2}{r} f_{jm}^{j+1}\right), \tag{A.26}$$

$$[\mathbb{D}_{\boldsymbol{f}}]_{jm}^{j+1,2} = -\sqrt{\frac{j+2}{2(2j+1)}}\left(\frac{\partial f_{jm}^{j}}{\partial r} - \frac{j}{r} f_{jm}^{j}\right), \tag{A.27}$$

$$[\mathbb{D}_{\boldsymbol{f}}]_{jm}^{j+2,2} = -\sqrt{\frac{j+2}{2j+3}}\left(\frac{\partial f_{jm}^{j+1}}{\partial r} - \frac{j+1}{r} f_{jm}^{j+1}\right). \tag{A.28}$$

A.3 Equations

In this last section of appendix, we give the final forms of the equations for elastic displacement, equations (1.10), and Navier-Stokes equations, given in equations (1.3). By using the expansions given in equations (A.1)- (A.3) and the formulas above, we can write the system given in equations (1.10) as in the following form

$$
\begin{aligned}
[\operatorname{div} \boldsymbol{u}]_{jm} &= 0, \\
[\operatorname{div} \mathbb{S}]_{jm}^{j-1} &= b_{jm}^{j-1}, \\
[\operatorname{div} \mathbb{S}]_{jm}^{j+1} &= b_{jm}^{j+1}, \\
S_{jm}^{j-2,2} - 2\mu\, [\mathbb{D}_{\boldsymbol{u}}]_{jm}^{j-2,2} &= 0, \\
S_{jm}^{j,2} - 2\mu\, [\mathbb{D}_{\boldsymbol{u}}]_{jm}^{j,2} &= 0, \\
S_{jm}^{j+2,2} - 2\mu\, [\mathbb{D}_{\boldsymbol{u}}]_{jm}^{j+2,2} &= 0.
\end{aligned}
\tag{A.29}
$$

The boundary conditions for this system, which are given in equations (1.12) and (1.13), are written as follows in terms of spherical harmonic coefficients, for top boundary of ice,

$$[\mathbb{S}\boldsymbol{e}_r]_{jm}^{j-1} = -\rho_i g \, [u_r \boldsymbol{e}_r]_{jm}^{j-1} ,$$
$$[\mathbb{S}\boldsymbol{e}_r]_{jm}^{j+1} = -\rho_i g \, [u_r \boldsymbol{e}_r]_{jm}^{j+1} ,$$
$$(A.30)$$

and for the bottom boundary of the ice shell

$$- [\mathbb{S}\boldsymbol{e}_r]_{jm}^{j-1} + (\rho - \rho_i)g \, [u_r \boldsymbol{e}_r]_{jm}^{j-1} = \rho \, [V\boldsymbol{e}_r]_{jm}^{j-1} ,$$
$$- [\mathbb{S}\boldsymbol{e}_r]_{jm}^{j+1} + (\rho - \rho_i)g \, [u_r \boldsymbol{e}_r]_{jm}^{j+1} = \rho \, [V\boldsymbol{e}_r]_{jm}^{j+1} .$$
$$(A.31)$$

The tidal potential given in equation (1.5), in terms of spherical harmonics coefficients, is given as

$$b_{jm}^{j-1} = \rho_i r\omega^2 e\sqrt{18\pi} \cos\omega t,$$
$$b_{jm}^{j+1} = -\rho_i r\omega^2 e \left(\sqrt{27\pi} \cos\omega t - i\sqrt{48\pi} \sin\omega t \right).$$
$$(A.32)$$

Tidal potential has only components for degree 2, and order 0 and 2, therefore the elastic equations (A.29) are only solved for these degree and orders, by the method prescribed in Section 1.4. The solution to system is then prescribed as the boundary condition for the Navier-Stokes equations (1.3). The solution to this system can be found separately for each order, because the systems are independent of each other for each degree. The normal component of the displacement $\boldsymbol{u}$ is then found for the degree 2, order 0 and 2 as given in Figure A.1 for one period. The radial displacement is found 1 m on average for 20 km thick of ice shell.
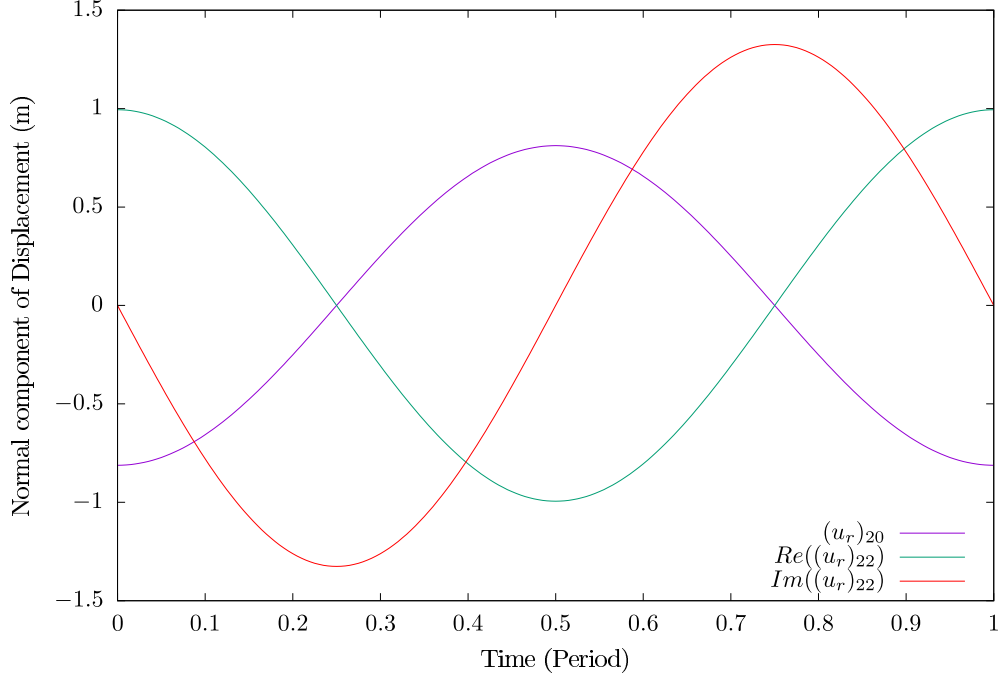
Figure A.1: Normal component of the displacement of the elastic ice shell, found for degree 2, order 0 and 2.

Finally, we can write the Navier-Stokes equations (1.3) in terms of spheroidal and toroidal parts. The spheroidal part of the system is given as

$$
[\operatorname{div} \boldsymbol{v}]_{jm} = 0,
$$

$$
-\frac{\partial v_{jm}^{j-1}}{\partial t} + [\operatorname{div} \mathbb{T}]_{jm}^{j-1} = b_{jm}^{j-1} - (f_c)_{jm}^{j-1},
$$

$$
-\frac{\partial v_{jm}^{j+1}}{\partial t} + [\operatorname{div} \mathbb{T}]_{jm}^{j+1} = b_{jm}^{j+1} - (f_c)_{jm}^{j+1},
$$

$$
T_{jm}^{j-2,2} - 2\eta \left[\mathbb{D}_{\boldsymbol{v}}\right]_{jm}^{j-2,2} = 0, \tag{A.33}
$$

$$
T_{jm}^{j,2} - 2\eta \left[\mathbb{D}_{\boldsymbol{v}}\right]_{jm}^{j,2} = 0,
$$

$$
T_{jm}^{j+2,2} - 2\eta \left[\mathbb{D}_{\boldsymbol{v}}\right]_{jm}^{j+2,2} = 0,
$$

and the toroidal part of the system is given by

$$
-\frac{\partial v_{jm}^{j}}{\partial t} + [\operatorname{div} \mathbb{T}]_{jm}^{j} = -(f_c)_{jm}^{j},
$$

$$
T_{jm}^{j-2,j-1} - 2\eta \left[\mathbb{D}_{\boldsymbol{v}}\right]_{jm}^{j-2,j-1} = 0, \tag{A.34}
$$

$$
T_{jm}^{j,j+1} - 2\eta \left[\mathbb{D}_{\boldsymbol{v}}\right]_{jm}^{j,j+1} = 0.
$$

The system given in equations (A.33) and (A.34) are no longer independent for degree and orders, due to the Coriolis force. Therefore, the Coriolis force term

is treated in explicit form in the time integration, given in equation (1.14). The boundary conditions for Navier-Stokes equations, which are given in equations (1.7), (1.8) and (1.9), are written in terms of spherical harmonic coefficients. For the bottom boundary of the ocean, given in equation (1.7), has the following form,

$$v_{jm}^l = 0, \tag{A.35}$$

both for spheroidal and toroidal part, i.e. $l = j - 1, j, j + 1$. The top boundary of the ocean, equation (1.8) has the form

$$[(\mathbb{T}\boldsymbol{e}_r) \cdot \boldsymbol{e}_r]_{jm} = - [\boldsymbol{u} \cdot \boldsymbol{e}_r]_{jm} (\rho - \rho_i)g, \tag{A.36}$$

and equation (1.9) has the form

$$v_{jm}^{j-1} - [(\boldsymbol{v} \cdot \boldsymbol{e}_r)\boldsymbol{e}_r]_{jm}^{j-1} = 0. \tag{A.37}$$

Note that, the equation (A.37) is only the one of the components of the vector, however it is linearly dependent with the other component, thus we take only this condition.